LA-11900-MS

UC-000
Issued: November 1990

LA--11900-MS

DE91 001618

Transionospheric Propagation Calculations for the Output of Two EMP Simulators

Robert Roussel-Dupré

Los Alamos ~~Los Alamos National Laboratory~~
Los Alamos,New Mexico 87545

TRANSIONOSPHERIC PROPAGATION CALCULATIONS FOR THE OUTPUT OF TWO EMP SIMULATORS

by

Robert Roussel-Dupré

Abstract

The Los Alamos Transionospheric Propagation Code (TIPC) was used to calculate the transionospheric signals corresponding to the computed output of two electromagnetic pulse (EMP) simulators, the NAVES II vertical polarization dipole and the TACAMO horizontal polarization dipole. The EMP calculations used as input to TIPC were performed by Mission Research Corporation. The 1986 International Reference Ionosphere code was used to generate vertical profiles of electron density over a twenty-four hour period for the geographical location of the NAVES II EMP simulator and for a solar activity projected for April, 1990, the original period of interest. A total electron content, used as input to TIPC, was calculated from the electron density profiles by integrating along a given line of sight. The maximum root mean square power densities to be expected in each of eight broadband receivers with bandwidths of 5 and 20 MHz centered at 200, 120, 80, and 40 MHz are presented.

I. INTRODUCTION

The purpose of this report is to present results of calculations performed at the request of AFTAC using the Los Alamos Transionospheric Propagation Code (TIPC) to obtain the transionospheric signal corresponding to the output of the NAVES II vertical polarization dipole (VPD) and the TACAMO horizontal polarization dipole (HPD) as computed by Ed Savage and Neal Carron of Mission Research Corporation (MRC). A brief description of the output pulses is given in Section II while the model ionosphere used for these calculations is presented in Section III. The maximum RMS power density to be expected in each of eight broadband receivers with bandwidths of 5 and 20 MHz centered at 200, 120, 80, and 40 MHz was calculated for TECs ranging from $0.0001-20 \times 10^{17}$ m^{-2}. The results are discussed in Section IV and a summary with recommendations is provided in Section V.

17 May 1990, Contract No. F62400-90-0034.
Prepared for Headquarters, AFTAC, Patrick AFB, FL 32925

II. OUTPUT OF HPD AND VPD DEVICES

The output of the NAVES II VPD was computed by MRC for two cases corresponding to a path over the ground with a conductivity and permittivity appropriate for 10% water content (labelled L01) and one over the sea with conductivity of 4 mhos/m and dielectric constant of 81 (labelled L02). Azimuthal directions that include paths over both ground and sea will yield signal strengths intermediate to the two cases considered. Calculations were provided in each case for fourteen elevation angles including 5, 9, 13, 17, 21, 25, 30, 34, 38, 42, 50, 58, 67, and 79 degrees. We chose to work with the pulses generated for propagation both over the ground and over the sea at three angles, namely, 17, 30, and 42 degrees. The temporal and spectral pulse shapes at 1000 km range for these six cases are shown in Figures 1a–f (L01) and 2a–f (L02). With the exception of minor bumps in the spectrum from 10–100 MHz of the L01_42 pulse (see Figure 1b), the spectral shape of these pulses can be characterized above 30 MHz as a monotonically decreasing function of frequency with no particularly interesting or identifying features. This fact suggests that except for the consideration of optimizing signal-to-noise ratios including ionospheric effects, the selection of particular frequency channels above 30 MHz is arbitrary. While optimizing signal strength favors the lower frequencies, minimizing ionospheric effects will favor the higher frequencies.

The output of the TACAMO HPD was computed by MRC for four elevation angles including 10, 20, 40, and 70 degrees and for four azimuthal directions measured with respect to the simulator arms, including 11.3, 37.5, 63.8, and 90 degrees. We chose to work with two pulses generated for propagation at 20° elevation and azimuthal angles with respect to the simulator arms of 37° and 90° (designated E20A37 and E20A90 respectively). Because of the four-fold azimuthal symmetry inherent to this configuration, calculations for the 37° azimuth correspond to geographical azimuths of 41, 116, 221, and 296 degrees while those for 90° azimuth correspond to geographical azimuths of 169° and 349°. The temporal and spectral pulse shapes projected back to one meter range for these two cases are shown in Figures 3a–b and 4a–b. The spectral shape of these signals shows an oscillatory structure that is associated with the interference of direct line of sight signal components and ground reflections. These oscillations occur above 10 MHz and have nulls at approximately 10 MHz intervals. This fact suggests that careful selection of operating frequencies will be necessary for bandwidths less than 10 MHz in order to insure adequate signal-to-noise. We note that the significant structure in the spectrum of this signal precludes a continuous measurement of the chirp rate of the transionospheric signal thereby making it more difficult to obtain an accurate ionospheric TEC.

III. IONOSPHERIC MODEL

The 1986 International Reference Ionosphere (IRI; Rawer *et al.*, 1978a and b; Bilitza, 1986; Rawer and Bradley, 1987) is a computer program that generates vertical profiles of electron density, electron and ion temperatures, and positive ion composition for any given geographical location, time of day, season and solar activity. The electron density profile is computed by interpolating a series of tables developed from synoptic measurements obtained with ionosondes, topside sounders and incoherent scatter radars. The data base in some cases constitutes more than 20 years of measurements taken on an hourly basis. IRI therefore represents an excellent tool for estimating average ionospheric conditions for a wide range of geographical locations in the northern hemisphere.

The input parameters to IRI include the geographical location (north latitude and east longitude), the sunspot number (available from the Geomagnetic and Solar Data published monthly by the *Journal of Geophysical Research*), the month, time of day (hour), solar inclination (can be computed internally by IRI), lower and upper limits of the height profile, and the profile height resolution. The output includes plots and a listing of the ionospheric constituents and electron and ion temperatures as a function of height. The electron density profile can then be integrated to yield the total electron content (TEC).

This code was used to generate electron density profiles and TECs for the geographical location of the NAVES II VPD (38° 15' N, 76° 20' W) and the solar activity projected for April, 1990. On the basis of the evolution over the past three years of solar cycle 22, the National Geophysical Data Center has predicted the sunspot number for April, 1990 to be 182 ± 34 at the 90% confidence level. We have generated the electron density profiles expected over Patuxent River, MD for a 24 hour period and for sunspot numbers of 150, 182, and 216. These profiles were then integrated for elevation angles of 90, 45, 30 and 15 degrees to obtain the corresponding TECs. Typical nighttime and daytime electron density profiles for a sunspot number of 182 are shown in Figures 5a and b, respectively. The TECs as a function of the time of day for each of the sunspot numbers and elevation angles discussed above are shown in Figures 6a–l. These calculations indicate an overall TEC range from approximately 1–30 × 10^{17} m^{-2} and an average day to night contrast in TEC of approximately a factor of three.

IV. TRANSIONOSPHERIC PROPAGATION

The transionospheric propagation code (TIPC; Roussel-Dupre and Kelley, 1989) was used to calculate the transionospheric signals corresponding to the pulses discussed in Section II for TECs ranging from 0.0001–20 × 10^{17} m^{-2}.

The result for the time domain signal L01_42.EVT from Savage and Carron and a TEC of 1×10^{17} m^{-2} is shown in Figure 7 for a frequency range from 40–500 MHz. The short rise in signal strength observed at the end of the pulses in these figures is a result of aliasing and should be ignored. Note that the signal strength does not vary substantially over the 7 μs length of the pulses. This result illustrates that ionospheric dispersion has reduced the amplitude of the low frequency components of the signal such that they are approximately equal to that of the high frequency components.

The transionospheric time domain signals corresponding to a TEC of 1×10^{17} m^{-2} are shown for the TACAMO HPD E20A37 and E20A90 pulses in Figures 8a–b for a frequency range from 37–500 MHz. Note that the strong oscillations in signal strength correspond to the arrival of individual frequency packets seen in the original signal spectrum, high frequencies arriving first. The strong variation in signal power versus frequency indicated in these results suggests that selection of operating frequencies would affect both signal-to-noise for detection and the measurement of TEC.

TIPC can also simulate the detection of signals by specified receivers. Eight receivers with central frequencies of 40, 80, 120, and 200 MHz and bandwidths of 20 and 5 MHz were modeled. The envelopes of the detected transionospheric signal for the VPD L02_17.EVT pulse are shown in Figures 9a - h for the 5 and 20 MHz bandwidth receivers centered at 120 MHz and for TECs of .01, 1, 5 and 20×10^{17} m^{-2}. Similar results are shown in Figures 10a–h for the HPD E20A37 pulse. For low TECs the filtered transionospheric signal has the shape essentially of the envelope of the impulse response of the filter. At high TECs the ionospheric dispersion dominates over the filter response and defines the shape of the detected signal.

The maximum RMS power density (watts/m^2) measured in each of these receivers at 1000 km range is plotted as a function of TEC (note that 1×10^{13} cm^{-2} = 1×10^{17} m^{-2}) for each of the NAVES II VPD pulses discussed in Section II (L01_42.EVT, L01_30.EVT, L02_42.EVT, L02_30.EVT, L02_17.EVT). The following figures give the responses to these signals at the indicated center frequencies: Figures 11a–l (200 MHz receiver); 12a–l (120 MHz receiver); 13a–l (80 MHz receiver); 14a–l (40 MHz receiver). Note that for large TEC the power varies inversely with TEC (*i.e.*, α 1/TEC) as expected. This fact can be used to extrapolate the results for TECs larger than those presented. To obtain the power at a range of R meters, multiply the value determined from the plots by $10^{12}/R^2$.

Similar results were obtained for each of the TACAMO HPD pulses discussed in Section II: (E20A37 and E20A90). The following figures give the responses to these signals at the indicated center frequencies: Figures 15a–d(200 MHz receiver); 16a–d (120 MHz receiver): 17a–d (80 MHz receiver); 18a–d (40 MHz receiver). To obtain the power at a range of R meters from these figures, multiply the value determined from the plots by $1/R^2$. Note that this normalization differs from that used for the VPD pulses.

V. SUMMARY

The spectral shape of the computed VPD pulses can be characterized above 30 MHz as a monotonically decreasing function of frequency with no particularly interesting or identifying features. The radiated power density in various spectral bands is summarized in Figures 19a and b for paths over the ground (L01) and over the sea (L02), respectively. For the elevation angles studied, the difference between the two paths is small (less than a factor of two in power density) and shows up primarily at low elevation angles (17°) and low frequencies (<80 MHz). The ratio of power density computed for a 20 MHz bandwidth receiver to that for a 5 MHz bandwidth receiver is approximately a factor of ten over the spectral range studied. Note that the source does not appear impulsive to receivers with bandwidths greater than or equal to 20 MHz, but that for narrower bandwidths it is reasonable to assume that the power density increases as the bandwidth squared. The spectral shape of the TACAMO HPD signals exhibits an oscillatory structure that is associated with the interference of direct line of sight signal components and ground reflections. These oscillations occur above 10 MHz and have nulls at approximately 10 MHz intervals. This fact suggests that careful selection of operating frequencies will be necessary for bandwidths less than 10 MHz in order to insure adequate signal-to-noise. The significant structure in the spectrum of this signal will make it more difficult to obtain an accurate ionospheric TEC. The radiated power density in various spectral bands is summarized in Figure 20 for two azimuthal directions(37°and 90°) measured relative to the axis of the simulator. As expected the power densities are higher across the spectral range at an azimuth of 90°.

The dominant effect of a deterministic ionosphere is to disperse the frequency content of an EMP in time with the high frequency components arriving first. The transionospheric signal computed for the VPD is stretched out over 7 μs in time for a TEC of 1×10^{17} m^{-2} with an amplitude that does not vary substantially with time (or frequency). This result illustrates that ionospheric dispersion has reduced the amplitude of the low frequency components of the signal such that it is approximately equal to that of the high frequency components. As a result, no optimum bandwidth exists for the VPD pulse assuming that the background noise is flat ('white') across the bandwidth. Receiver frequencies should be selected in spectral regions with minimum background noise. Similar results apply for the HPD pulse except for the additional amplitude modulation introduced by interference effects.

The maximum RMS power density (watts/m²) measured in each of eight receivers is plotted as a function of TEC in Figures 11–14 for each of the NAVES II VPD pulses and in Figures 15–18 for each of the TACAMO HPD pulses. A listing of the pulses, receivers and associated bandwidths, and corresponding figures is provided in Table I for convenience.

TABLE 1. PLOTS OF RMS POWER DENSITY VS. TEC

Pulse Type	Elevation (°)	Azimuth (°)	Receiver Frequency (MHz)	Bandwidth (MHz)	Figure Number
VPD	42	Ground	200	20	11a
VPD	42	Ground	200	5	11b
VPD	30	Ground	200	20	11c
VPD	30	Ground	200	5	11d
VPD	17	Ground	200	20	11e
VPD	17	Ground	200	5	11f
VPD	42	Sea	200	20	11g
VPD	42	Sea	200	5	11h
VPD	30	Sea	200	20	11i
VPD	30	Sea	200	5	11j
VPD	17	Sea	200	20	11k
VPD	17	Sea	200	5	11l
VPD	42	Ground	120	20	12a
VPD	42	Ground	120	5	12b
VPD	30	Ground	120	20	12c
VPD	30	Ground	120	5	12d
VPD	17	Ground	120	20	12e
VPD	17	Ground	120	5	12f
VPD	42	Sea	120	20	12g
VPD	42	Sea	120	5	12h
VPD	30	Sea	120	20	12i
VPD	30	Sea	120	5	12j
VPD	17	Sea	120	20	12k
VPD	17	Sea	120	5	12l
VPD	42	Ground	80	20	13a
VPD	42	Ground	80	5	13b
VPD	30	Ground	80	20	13c
VPD	30	Ground	80	5	13d
VPD	17	Ground	80	20	13e
VPD	17	Ground	80	5	13f
VPD	42	Sea	80	20	13g
VPD	42	Sea	80	5	13h
VPD	30	Sea	80	20	13i
VPD	30	Sea	80	5	13j
VPD	17	Sea	80	20	13k
VPD	17	Sea	80	5	13l

TABLE 1. CONT.

Pulse Type	Elevation (°)	Azimuth (°)	Receiver Frequency (MHz)	Bandwidth (MHz)	Figure Number
VPD	42	Ground	40	20	14a
VPD	42	Ground	40	5	14b
VPD	30	Ground	40	20	14c
VPD	30	Ground	40	5	14d
VPD	17	Ground	40	20	14e
VPD	17	Ground	40	5	14f
VPD	42	Sea	40	20	14g
VPD	42	Sea	40	5	14h
VPD	30	Sea	40	20	14i
VPD	30	Sea	40	5	14j
VPD	17	Sea	40	20	14k
VPD	17	Sea	40	5	14l
HPD	20	37	200	20	15a
HPD	20	90	200	5	15b
HPD	20	37	200	20	15c
HPD	20	90	200	5	15d
HPD	20	37	120	20	16a
HPD	20	90	120	5	16b
HPD	20	37	120	20	16c
HPD	20	90	120	5	16d
HPD	20	37	80	20	17a
HPD	20	90	80	5	17b
HPD	20	37	80	20	17c
HPD	20	90	80	5	17d
HPD	20	37	40	20	18a
HPD	20	90	40	5	18b
HPD	20	37	40	20	18c
HPD	20	90	40	5	18d

ACKNOWLEDGEMENTS

The author would like to thank Dr. Stephen Knox for helpful discussions and a critical review of this document.

REFERENCES

Bilitza, D., 1986, "IRI: Recent Developments," *Radio Sci.*, **21**, 343.

Rawer, K., D. Bilitza and S. Ramakrishnan, 1978a, *Rev. of Geophys. and Spa. Phys.*, **16**, No. 2, 177.

Rawer, K., S Ramakrishnan, and D. Bilitza, 1978b, "IRI 1978," International Union of RadioScience (URSI), Brussels, 75 pages.

Rawer, K. and P. A. Bradley 1987, editors of "International Reference Ionosphere—Status 1986/87," *Advances in Spa. Res.*, **7**, No. 6, 129 pages.

Roussel-Dupre, R. and Kelley, T. A. "Transionospheric Propagation Code (TIPC)," LAMS Report in press, Los Alamos National Laboratory, Los Alamos, New Mexico.

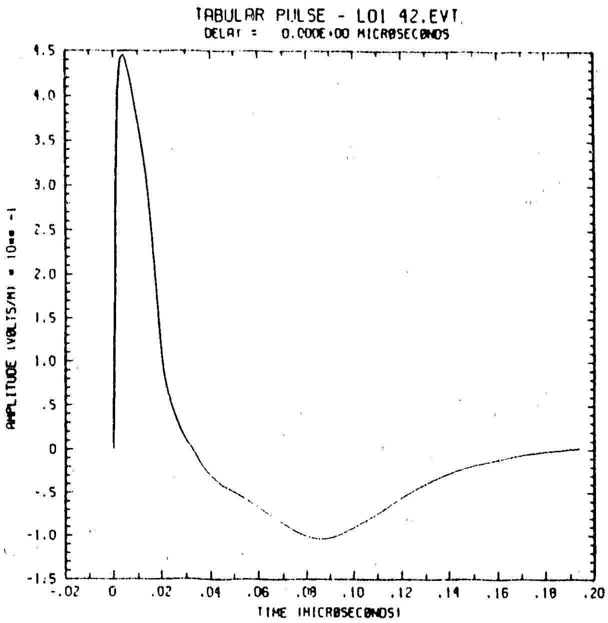

1a

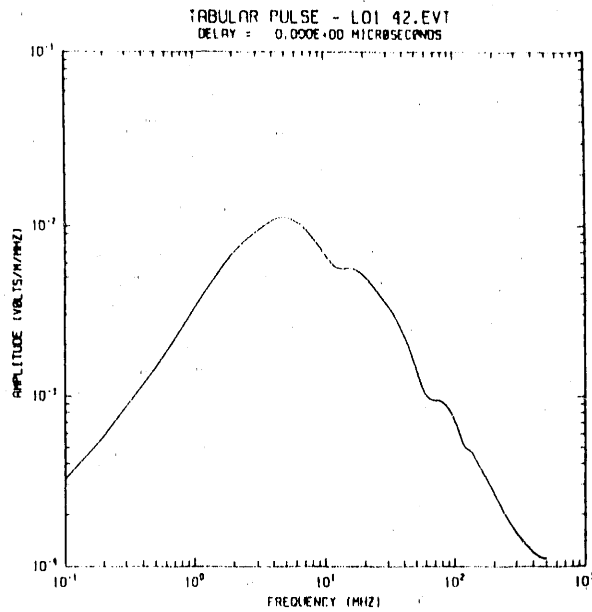

1b

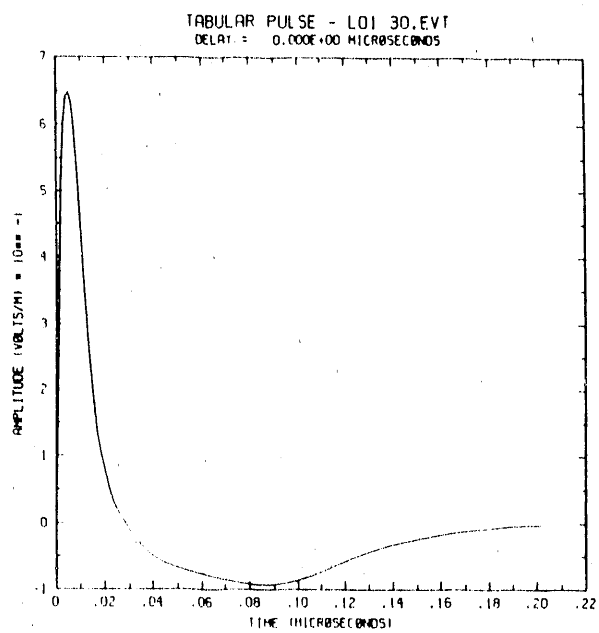

1c

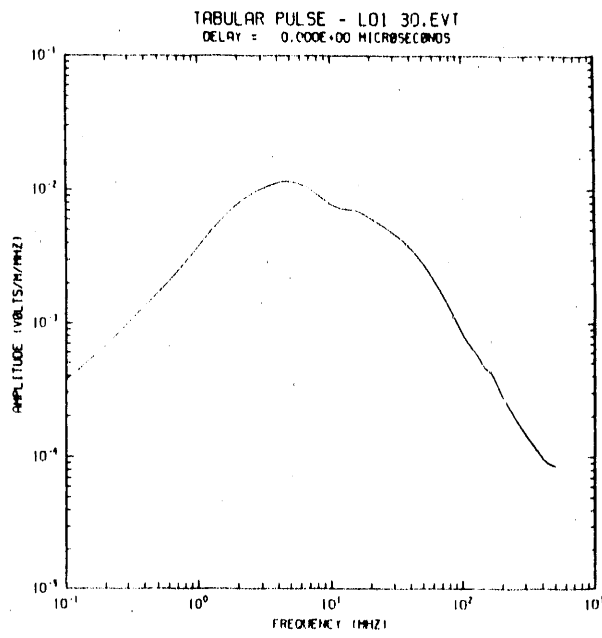

1d

Figures 1a–d: Plots of the temporal and spectral VPD L01 pulse shapes at 1000 km range for elevation angles of 17° (1a and b), and 30° (1c and d).

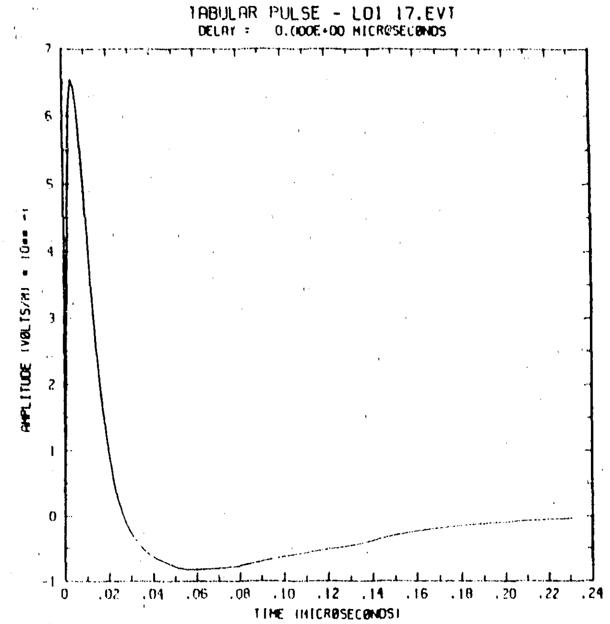

1c

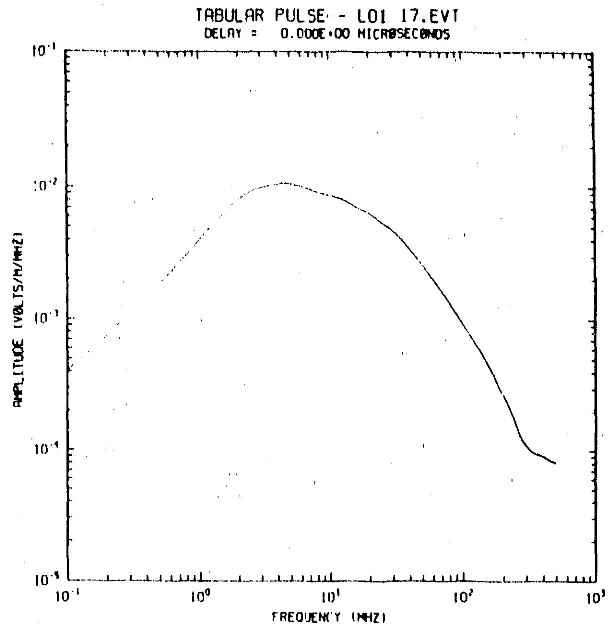

1f

Figures 1e–f: Plots of the temporal and spectral VPD L01 pulse shapes at 1000 km range for elevation angle of 42° (1e and f).

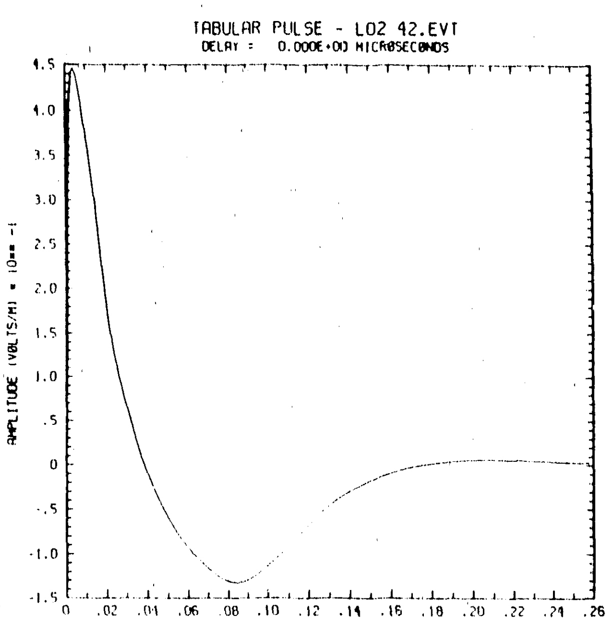

2a

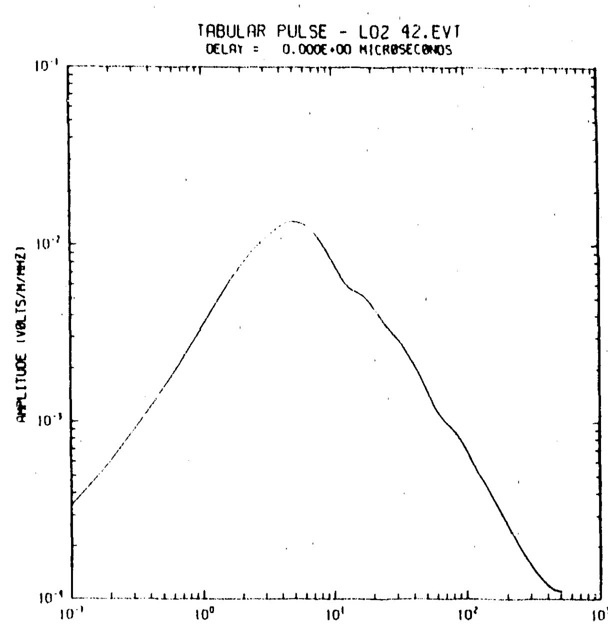

2b

Figures 2a–b: Plots of the temporal and spectral VPD L02 pulse shapes at 1000 km range for elevation angles of 17° (2a and b).

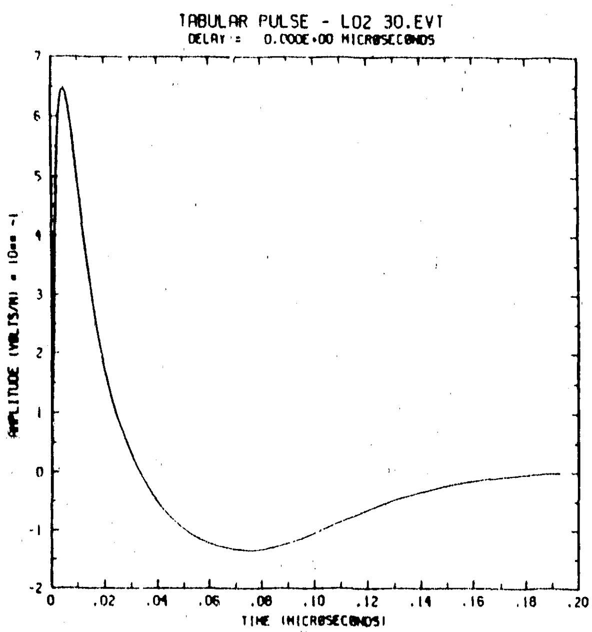

2c

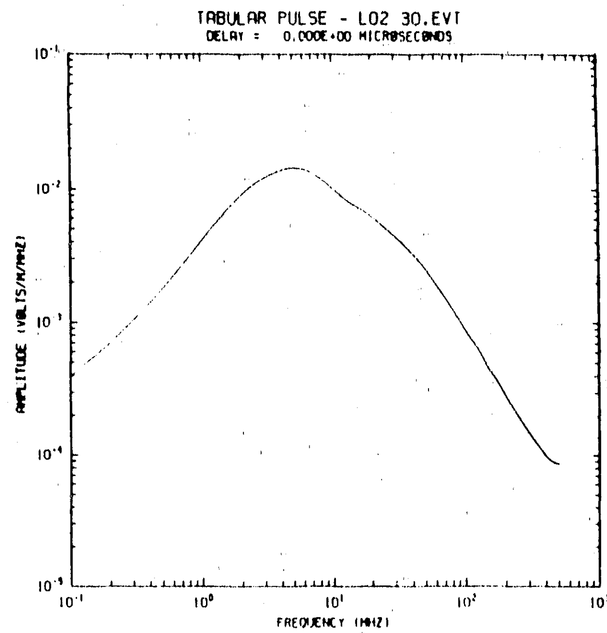

2d

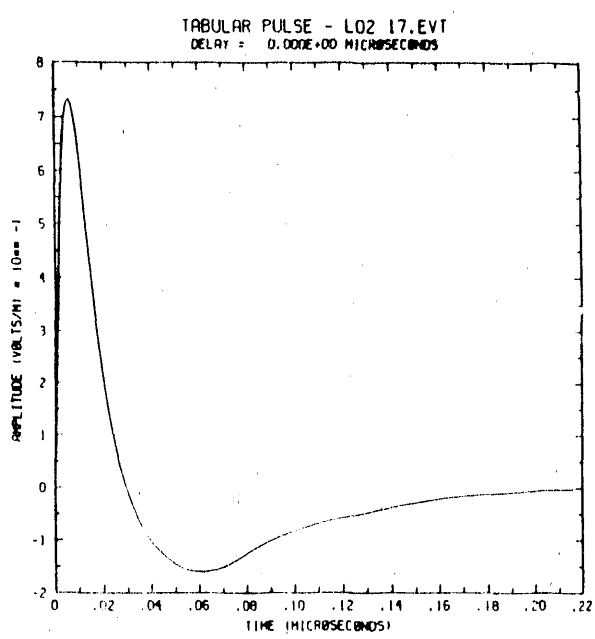

2e

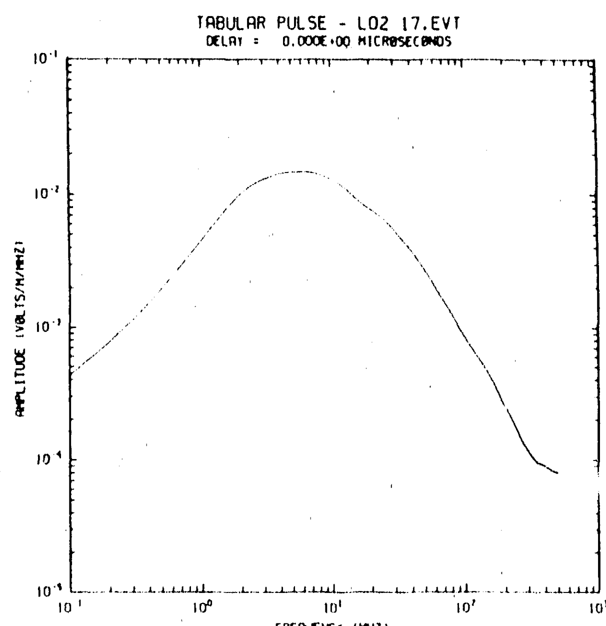

2f

Figures 2c–e: Plots of the temporal and spectral VPD L02 pulse shapes at 1000 km range for elevation angles of 30° (2c and d), and 42° (2e and f).

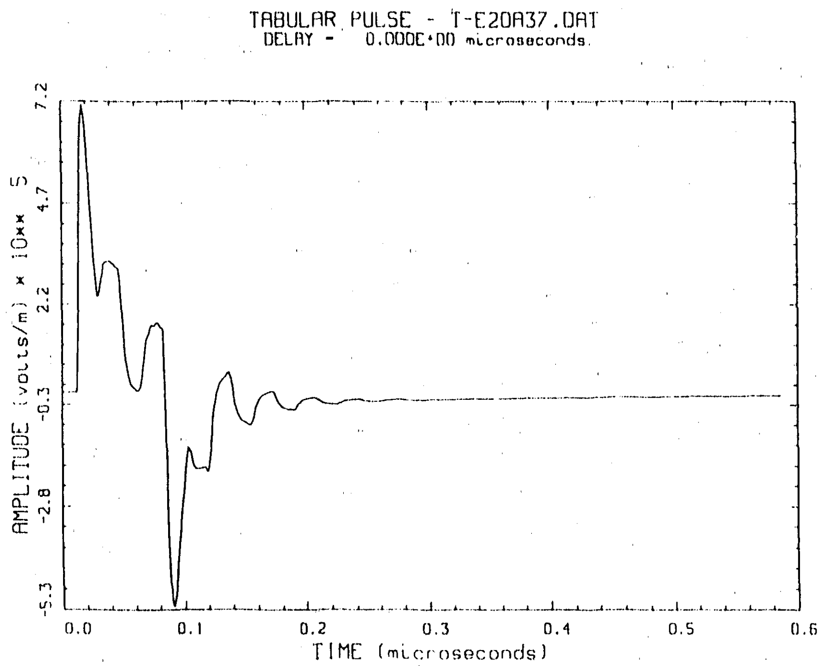

3a

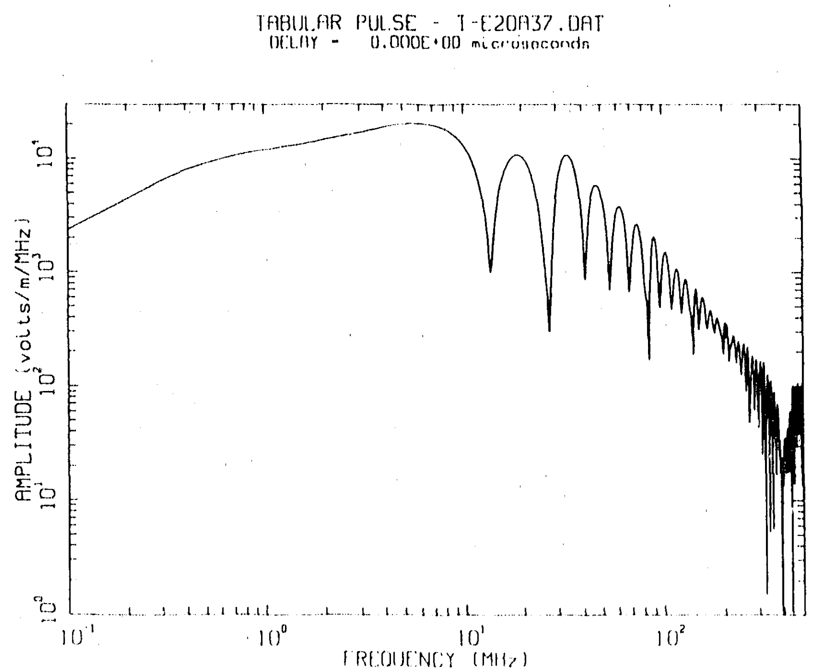

3b

Figures 3a–b: Plots of the temporal (a) and spectral (b) HPD pulse shapes at 1 m range for an elevation angle of 20° and an azimuthal direction measured with respect to the simulator arms of 37°.

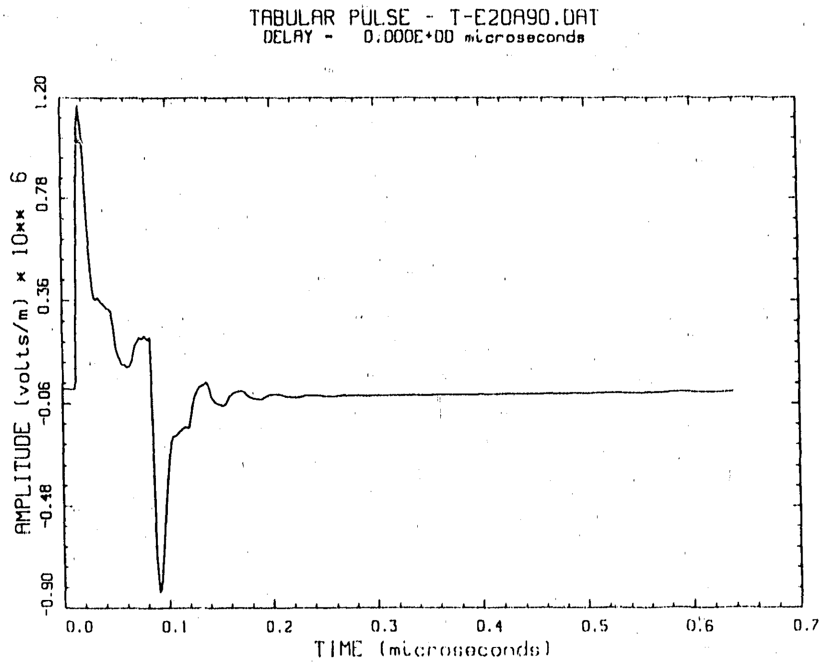

4a

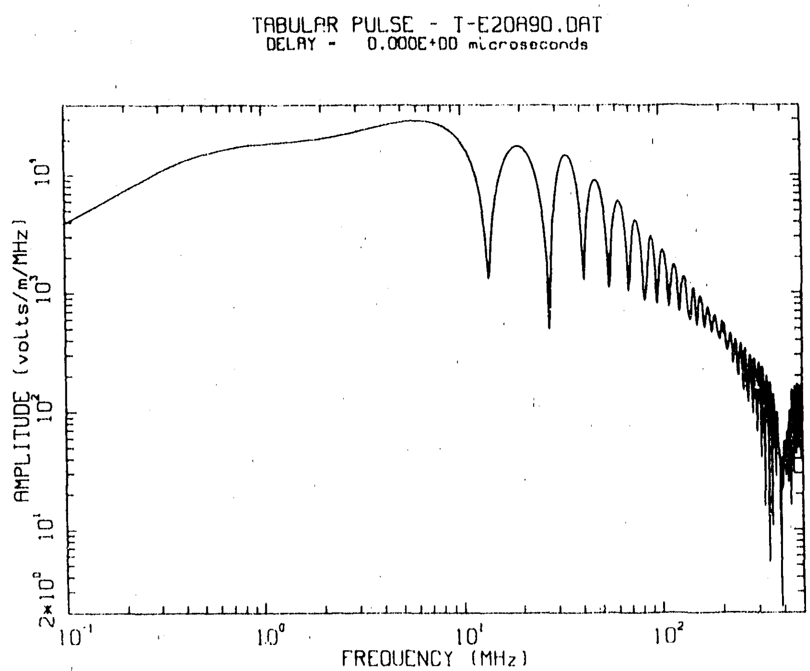

4b

Figures 4a–b: Plots of tl e temporal (a) and spectral (b) HPD pulse shapes at 1 m range for an elevation angle of 20° and an azimuthal direction measured with respect to the simulator arms of 90°.

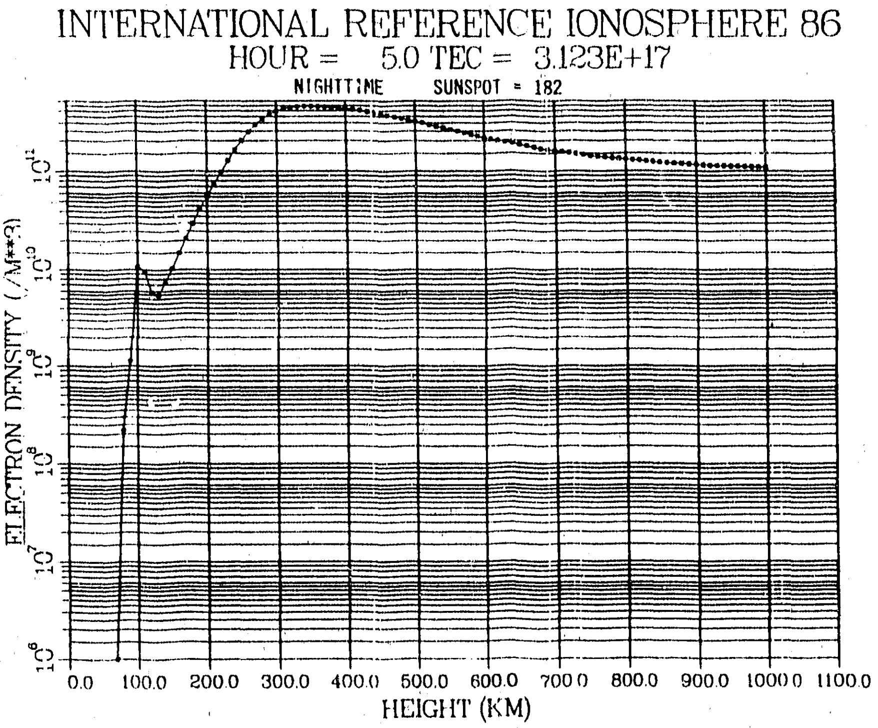

5a

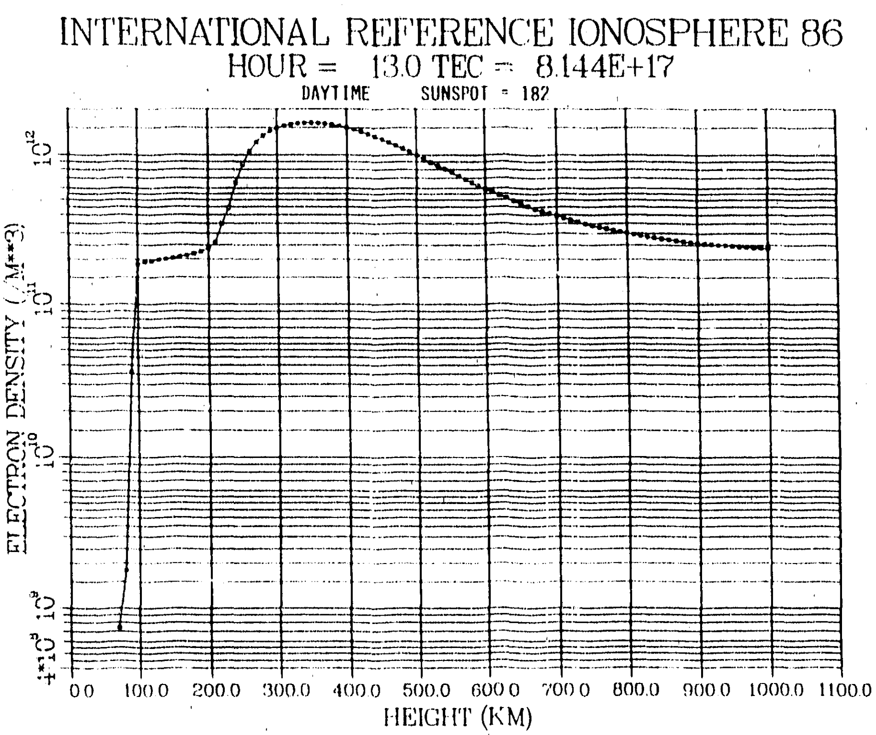

5b

Figures 5a-b: Typical nighttime (a) and daytime (b) electron density profiles over Patuxent River, MD for a sunspot number of 182.

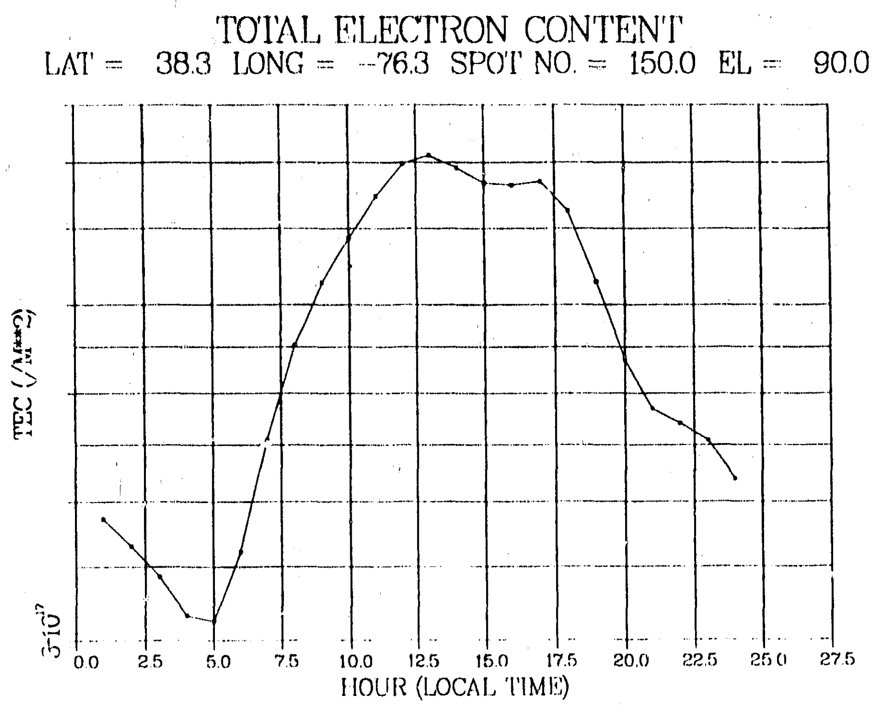

6a

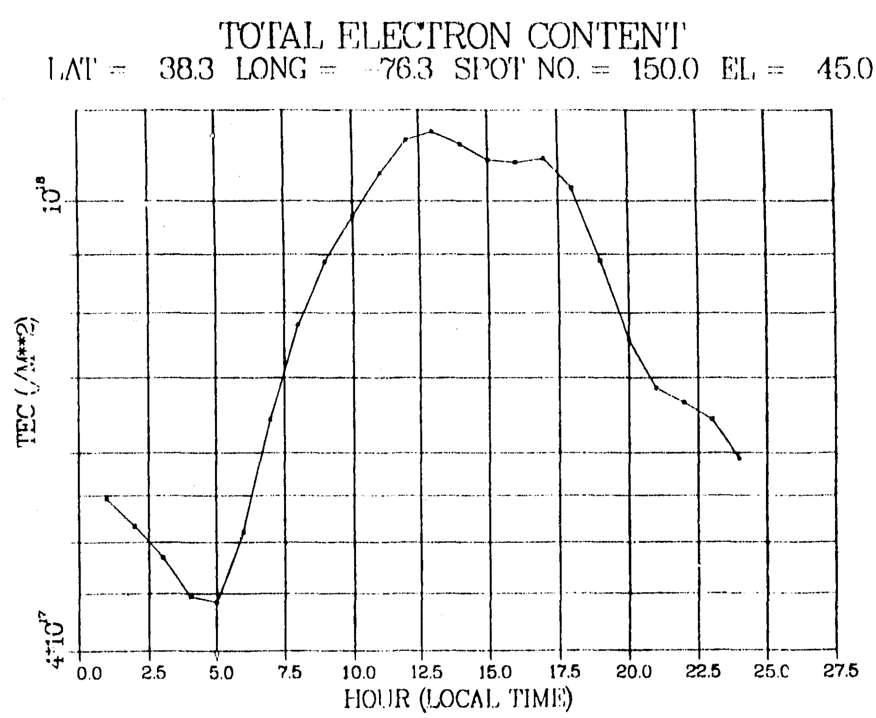

6b

Figures 6a–b: Plots of the TEC as a function of the time of day for sunspot numbers and elevation angles of 150, 90° (a); and 150, 45° (b).

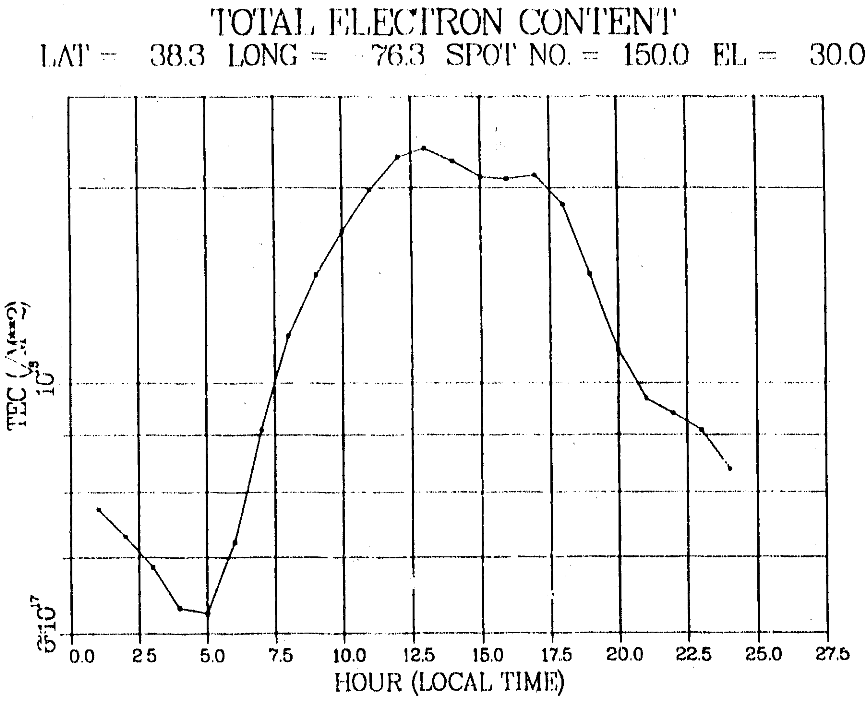

6c

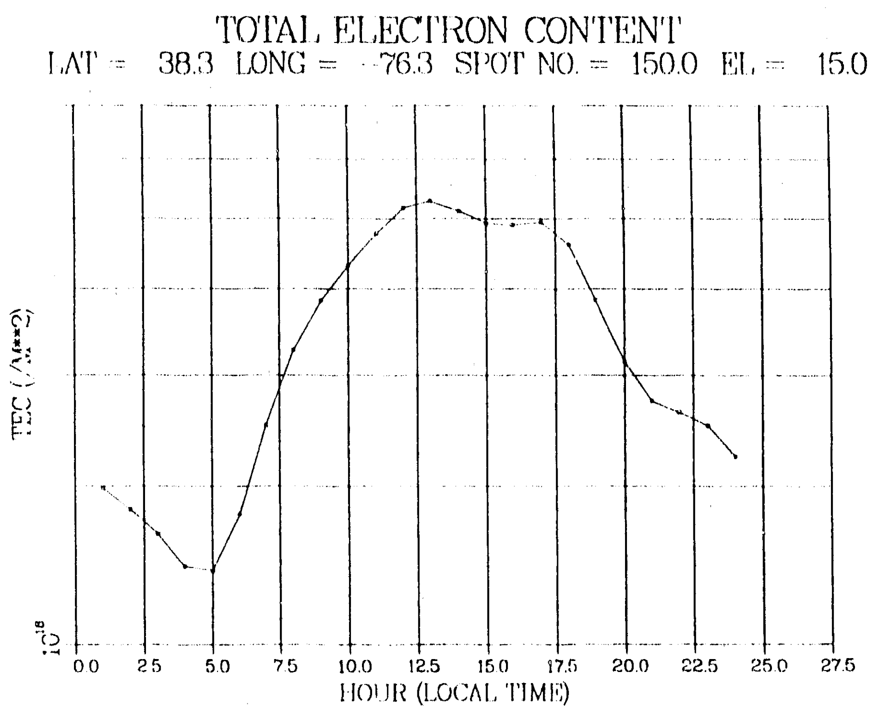

6d

Figures 6c–d: Plots of the TEC as a function of the time of day for sunspot numbers and elevation angles of 150, 30°(c); and 150, 15° (d).

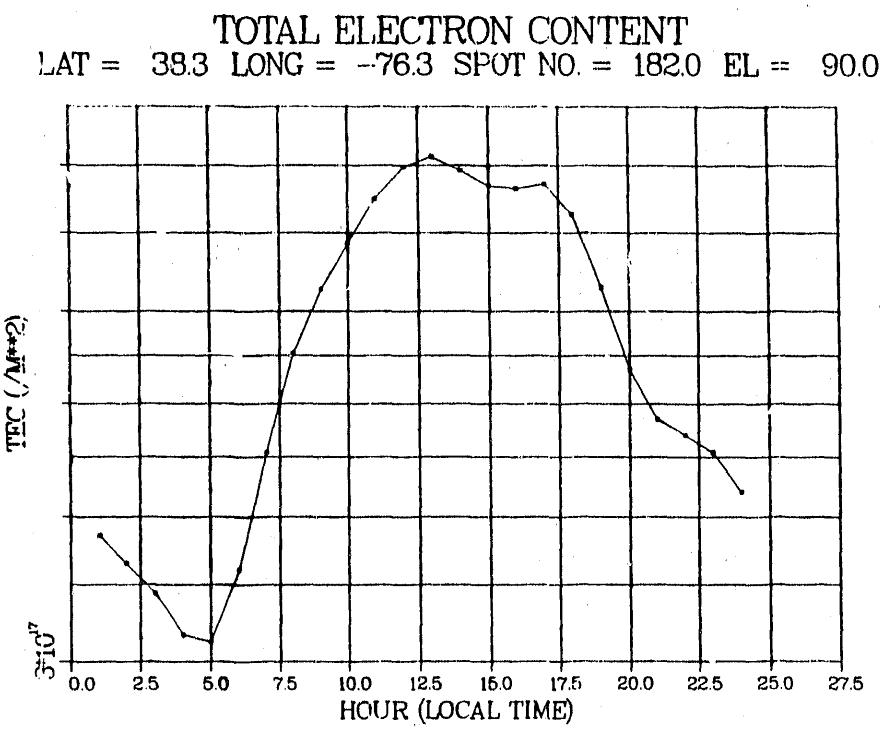

6e

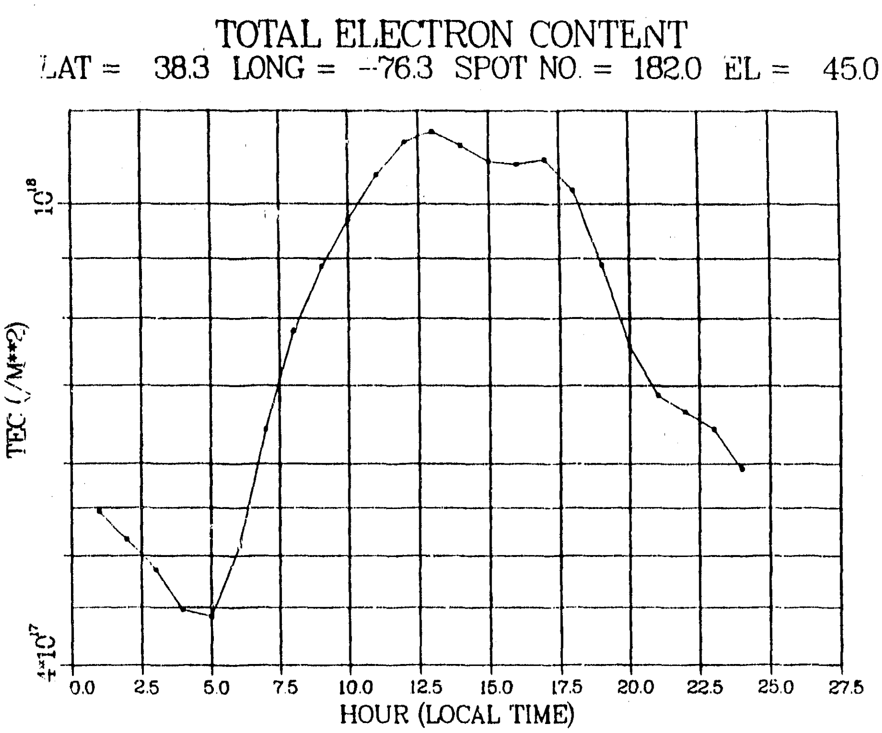

6f

Figures 6e–f: Plots of the TEC as a function of the time of day for sunspot numbers and elevation angles of 182, 90° (e); and 182, 45° (f).

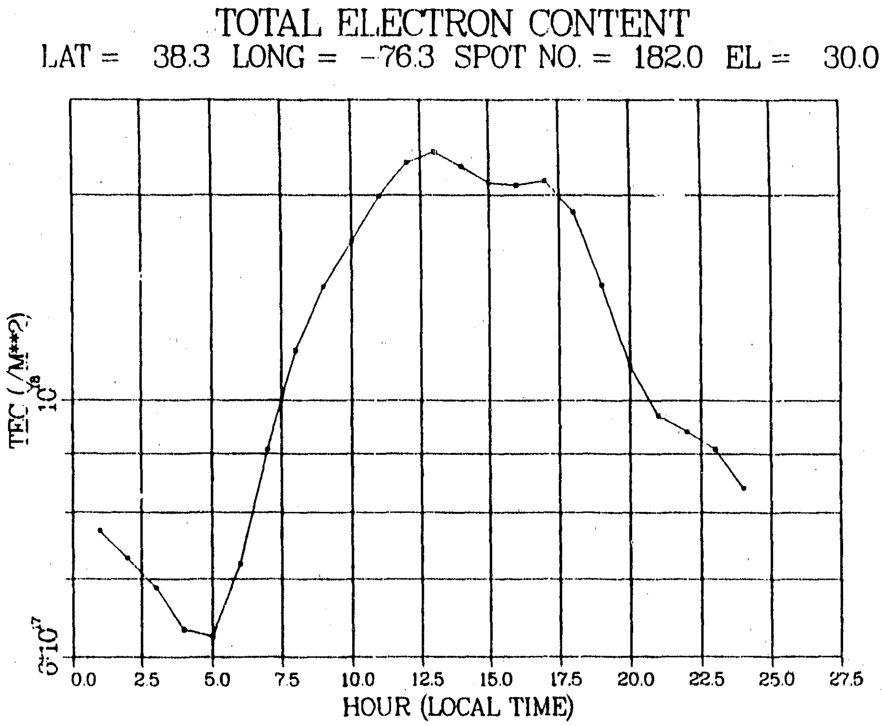

6g

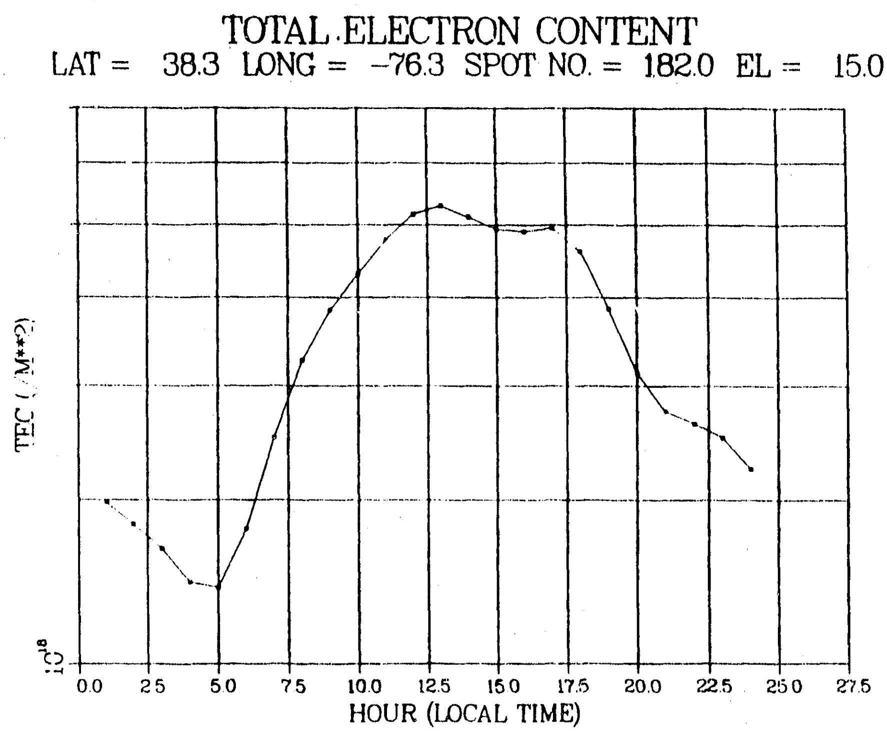

6h

Figures 6g–h: Plots of the TEC as a function of the time of day for sunspot numbers and elevation angles of 182, 30° (g).; and 182, 15° (h).

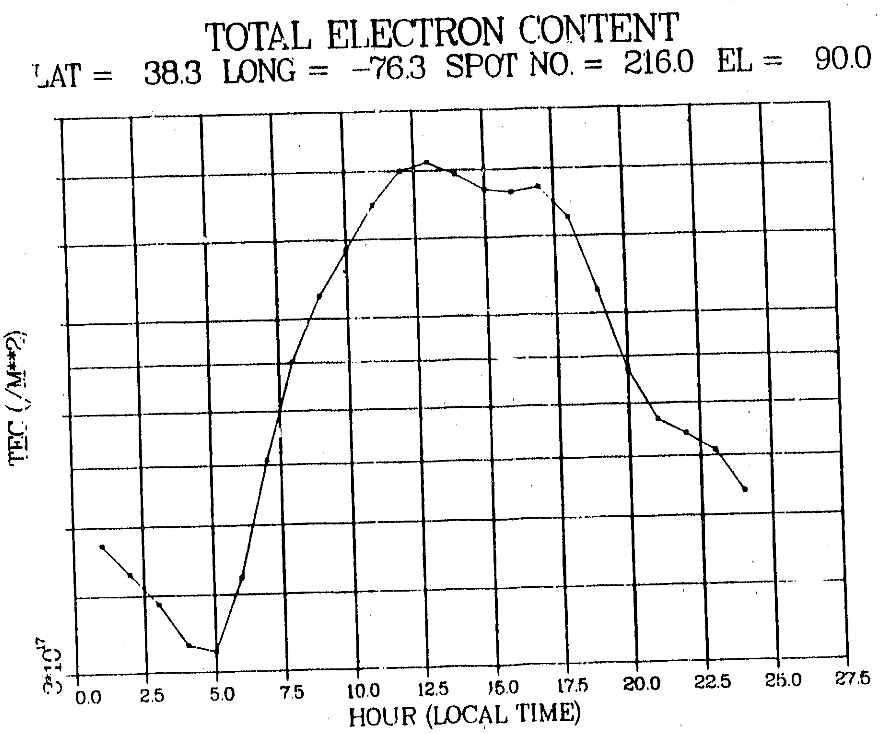

6i

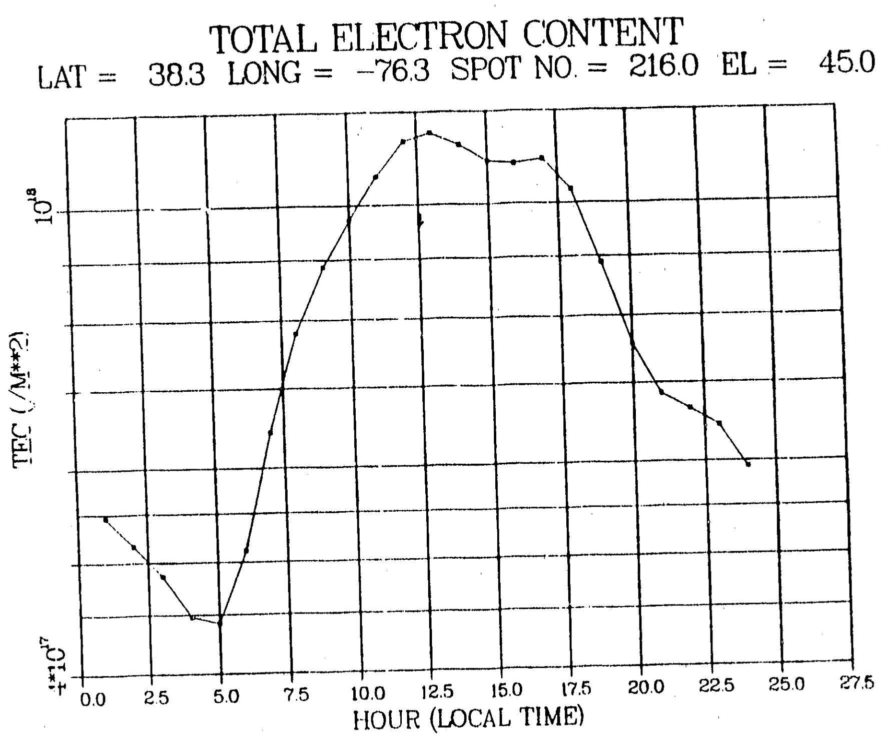

6j

Figures 6i–j: Plots of the TEC as a function of the time of day for sunspot numbers and elevation angles of 216, 90° (i); and 216, 45° (j).

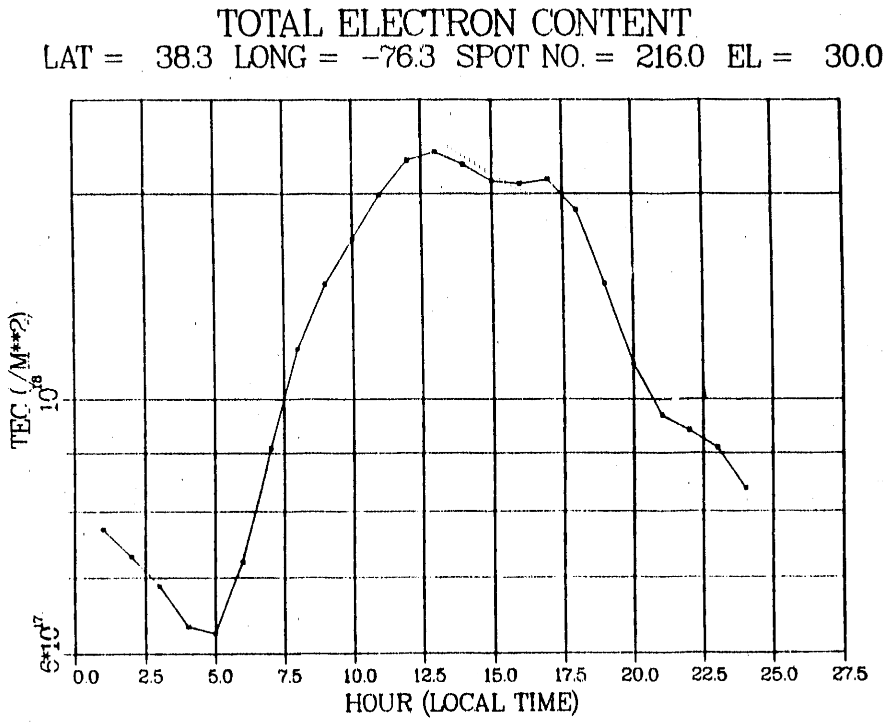

6k

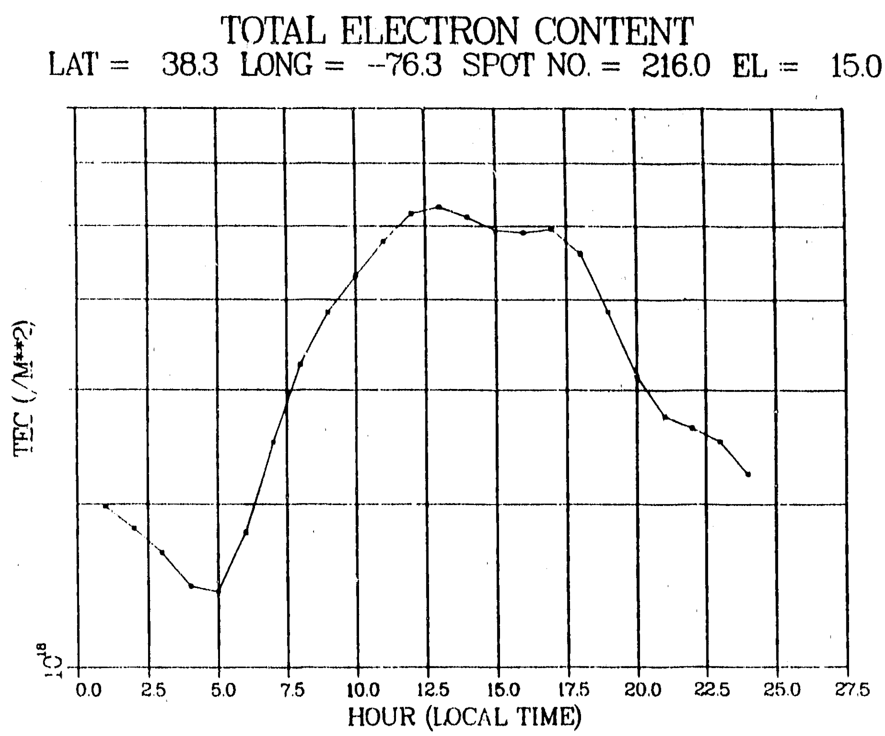

6l

Figures 6k–l: Plots of the TEC as a function of the time of day for sunspot numbers and elevation angles of 216, 30° (k); and 216, 15° (l).

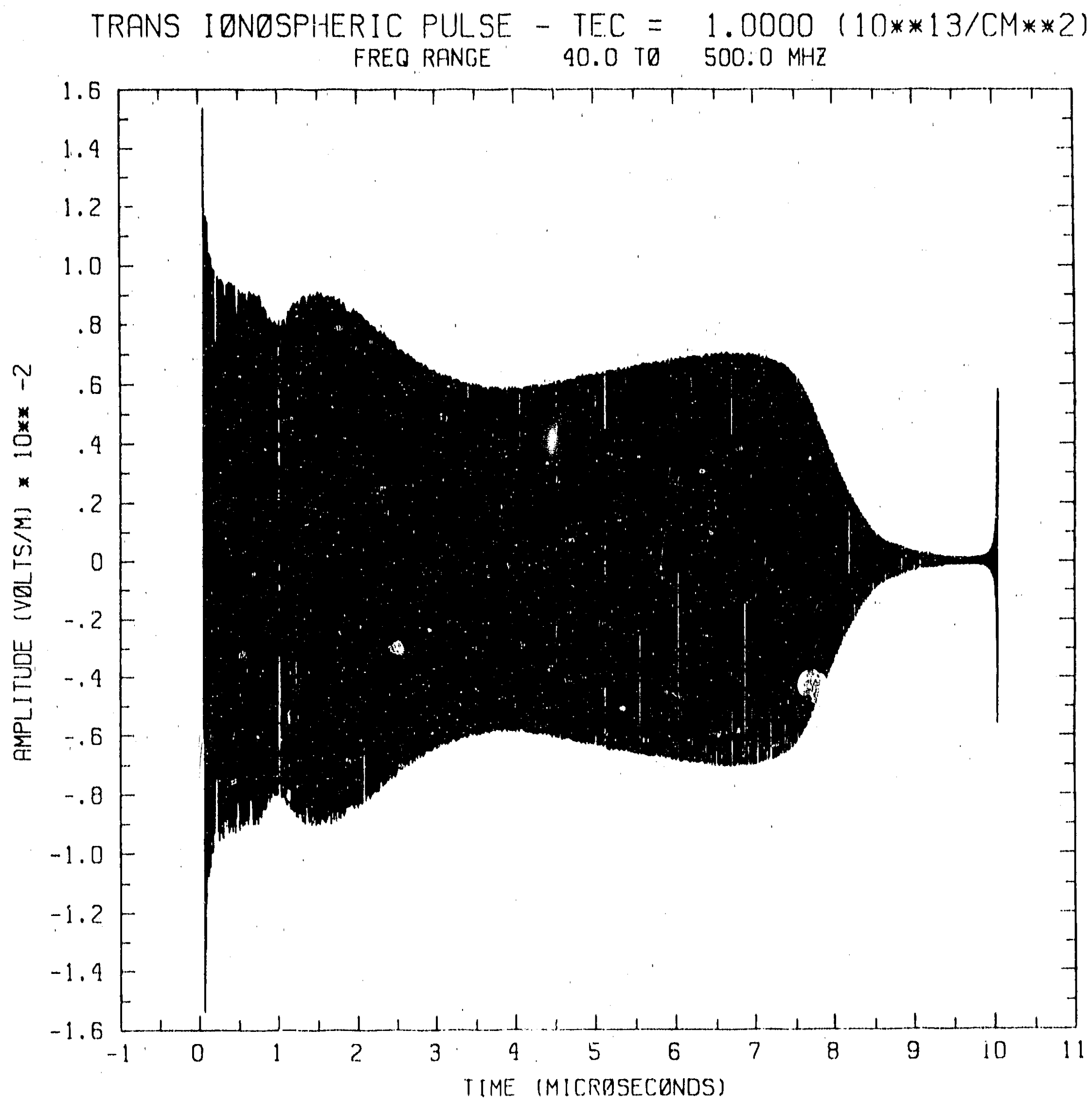

Figure 7: Transionospheric signal for the VPD L01 pulse at 42° elevation and for a TEC of 1×10^{17} m^{-2}. Only frequencies in the range of 40–500 MHz are included in this plot.

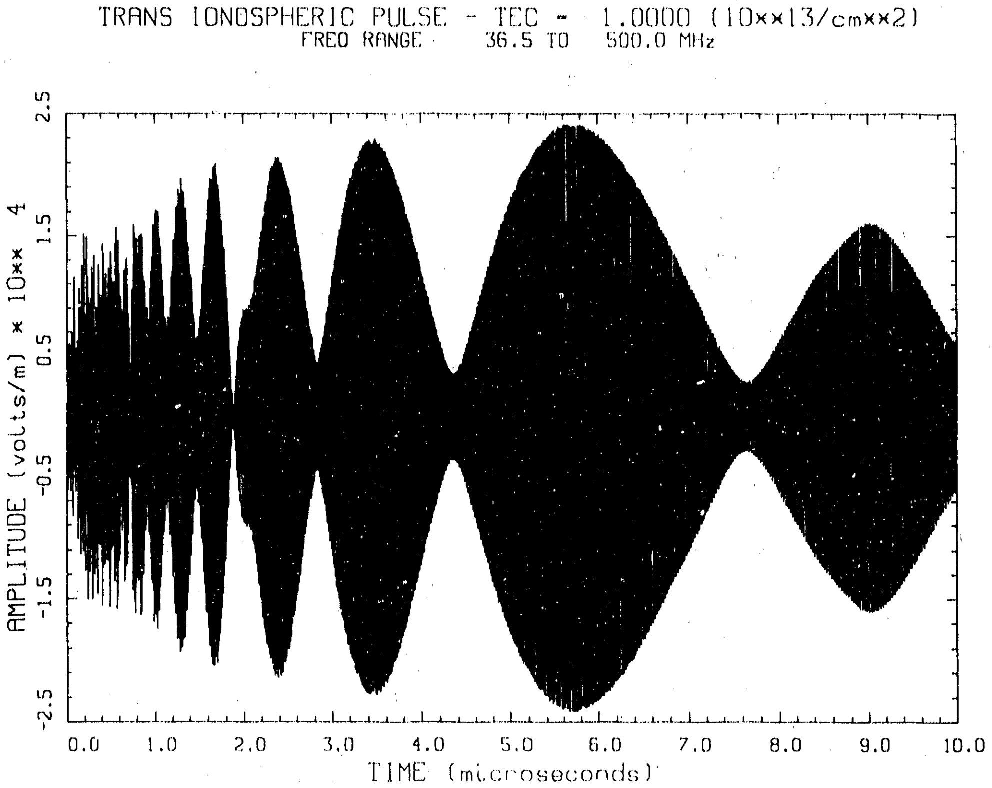

8a

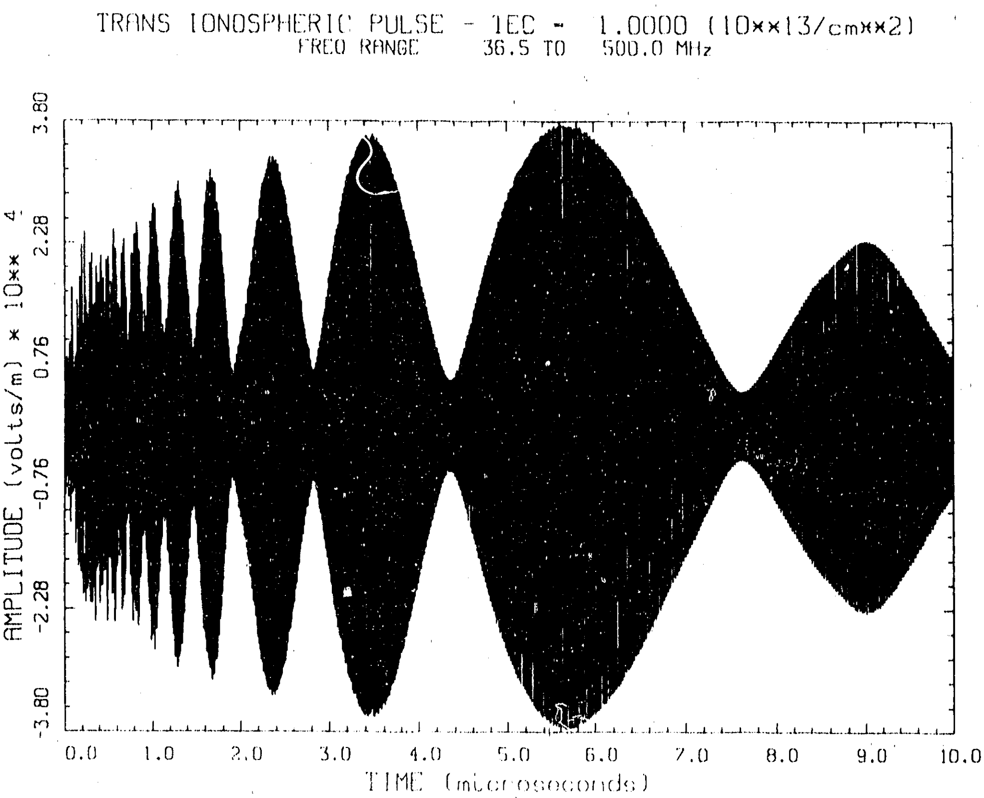

8b

Figures 8a–b: Transionospheric signals for the HPD pulses at 20° elevation, 37° azimuth (a) and 20° elevation, 90° azimuth (b), for a TEC of 1×10^{17} m^{-2}. Only frequencies in the range of 37–500 MHz are included in these plots.

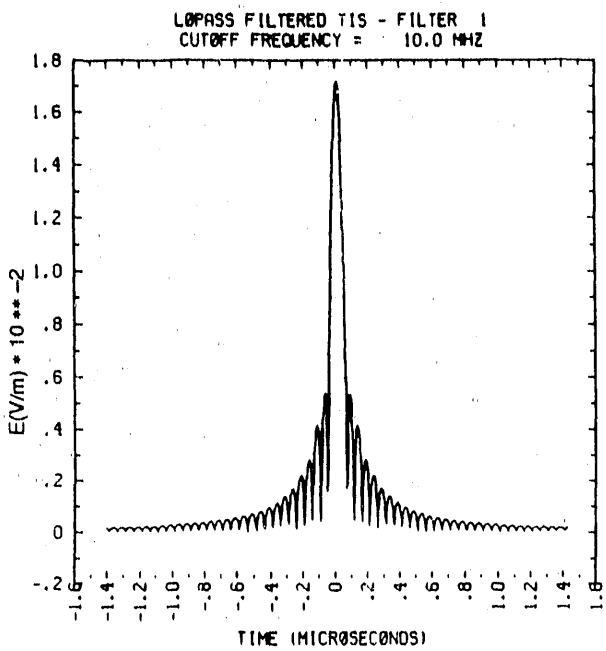

9a

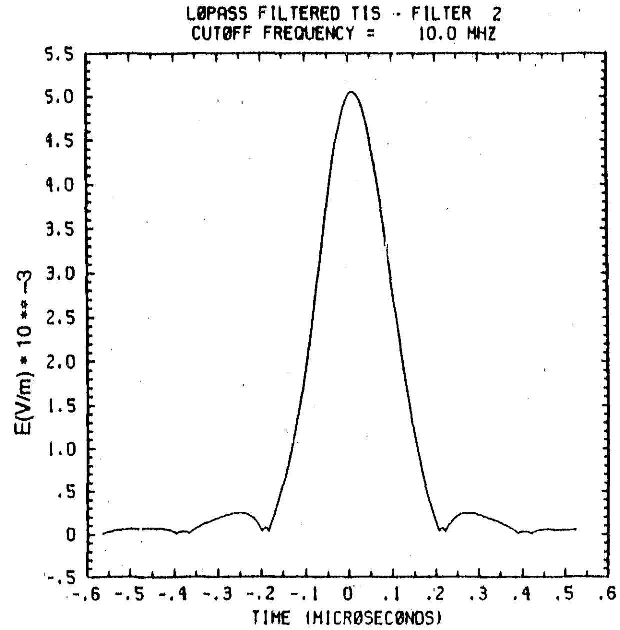

9b

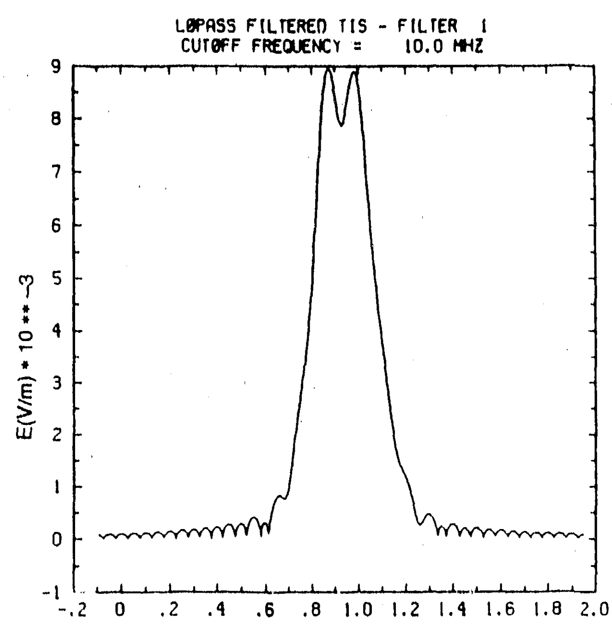

9c

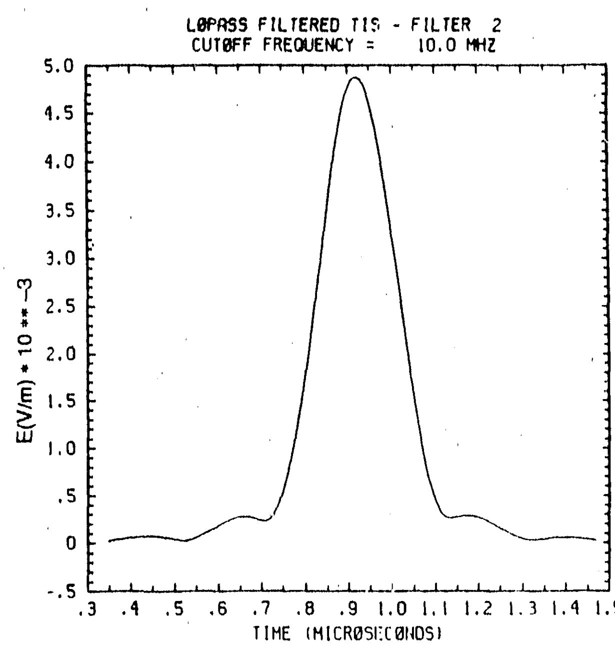

9d

Figures 9a–d: Envelopes of the detected transionospheric signal for the VPD L02 pulse at 17° elevation for the 5 and 20 MHz bandwidth receivers centered at 120 MHz and for TECs of 0.01×10^{17} m^{-2} (a and b), 1.0×10^{17} m^{-2} (c and d).

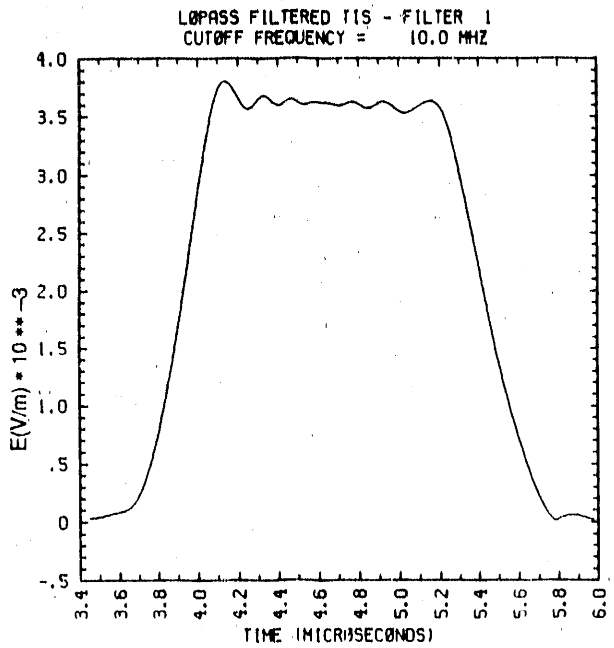

9e

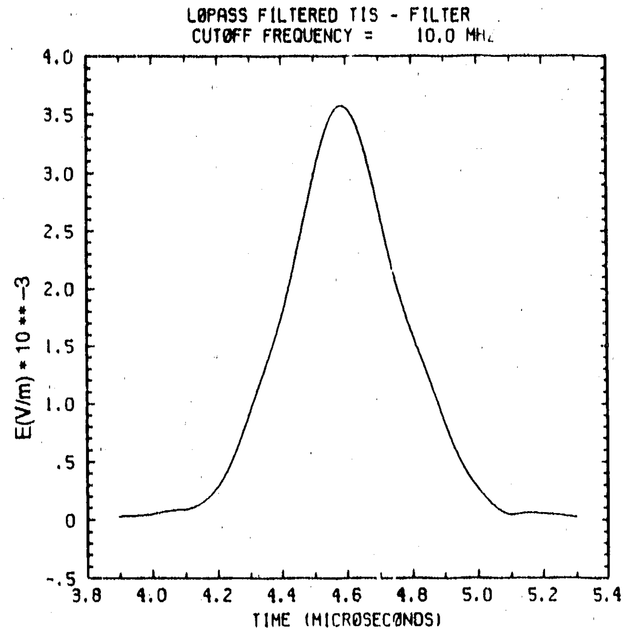

9f

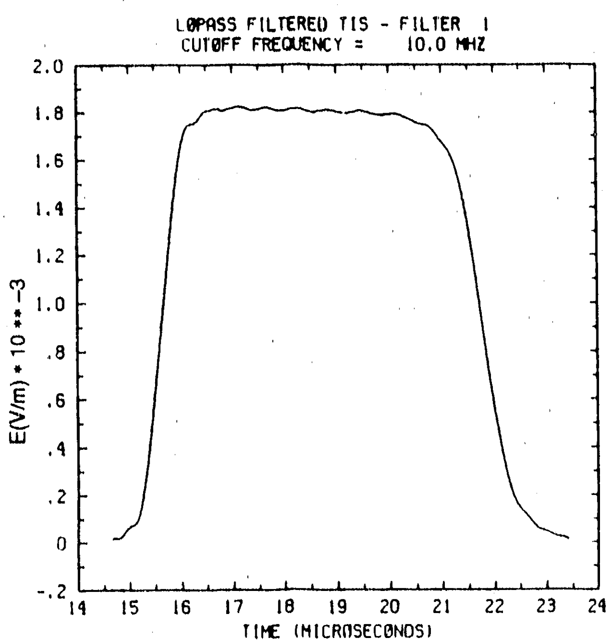

9g

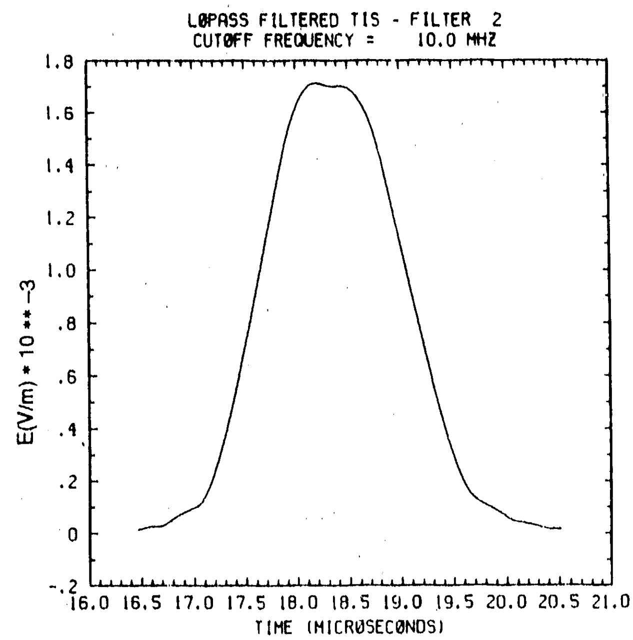

9h

Figures 9e–h: Envelopes of the detected transionospheric signal for the VPD L02 pulse at 17° elevation for the 5 and 20 MHz bandwidth receivers centered at 120 MHz and for TECs of 5.0×10^{17} m^{-2} (e and f), and 20.0×10^{17} m^{-2} (g and h).

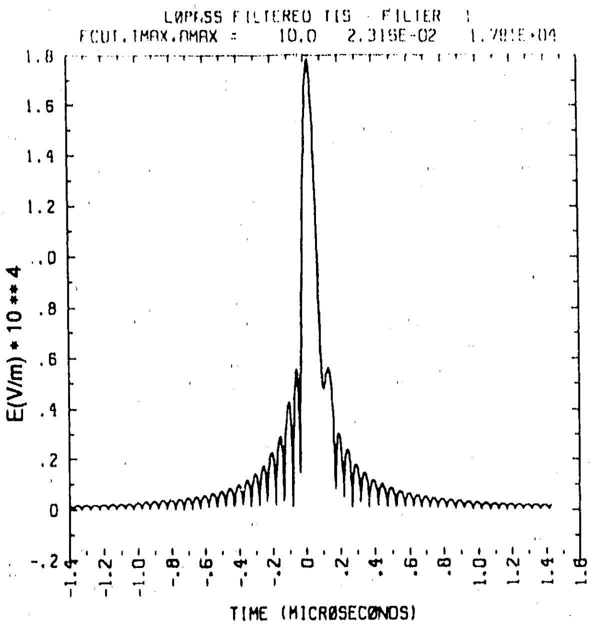

10a

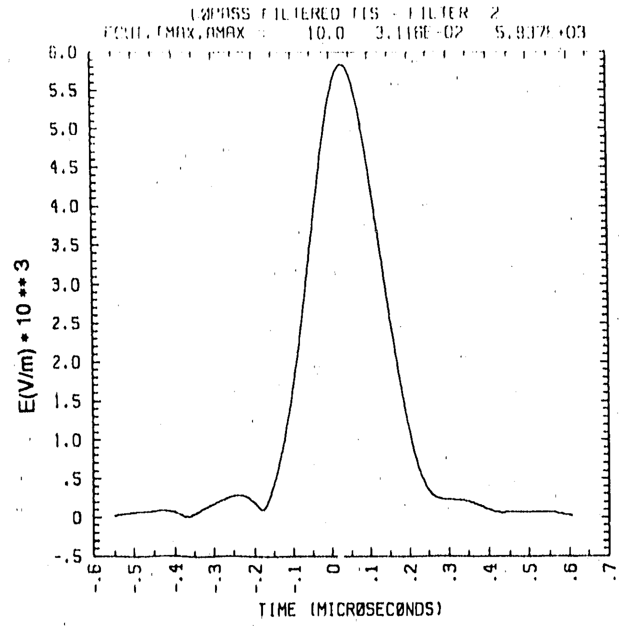

10b

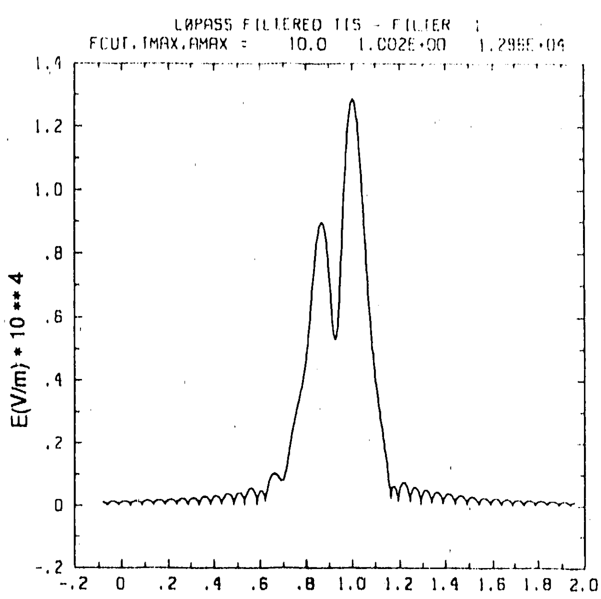

10c

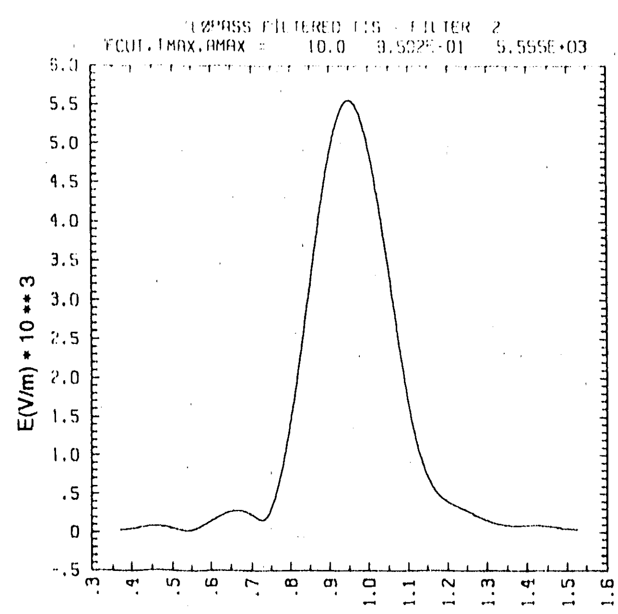

10d

Figures 10a–d: Envelopes of the detected transionospheric signal for the HPD pulse at 20° elevation and 37° azimuth for the 5 and 20 MHz bandwidth receivers centered at 120 MHz and for TECs of 0.01×10^{17} m^{-2} (a and b), 1.0×10^{17} m^{-2} (c and d).

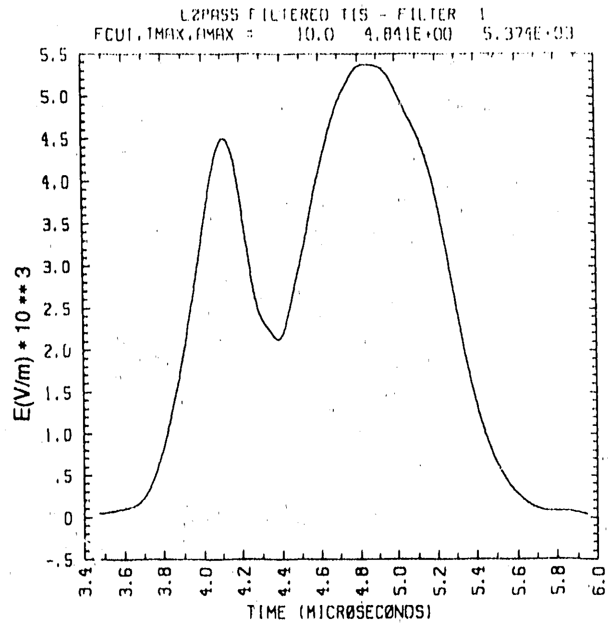

10e

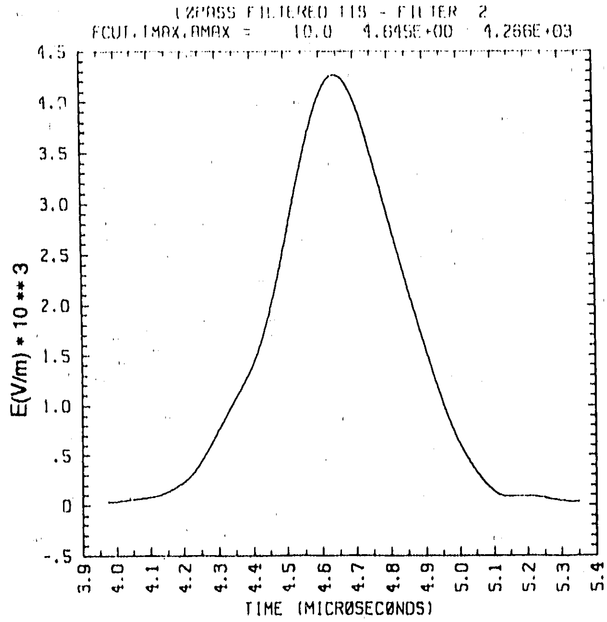

10f

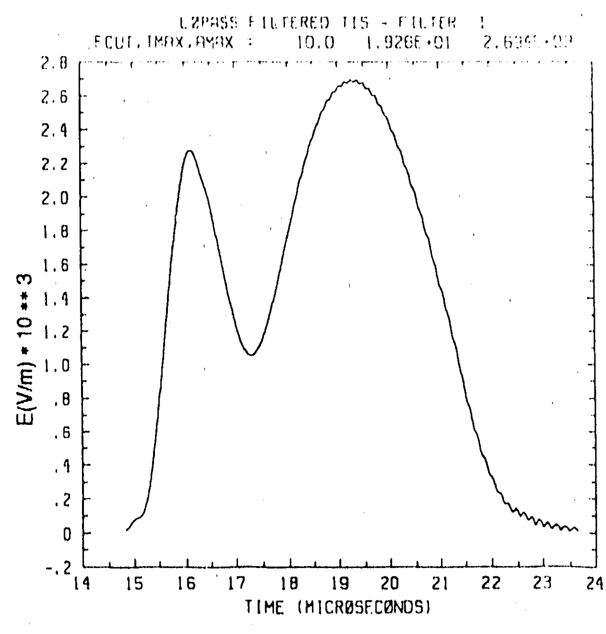

10g

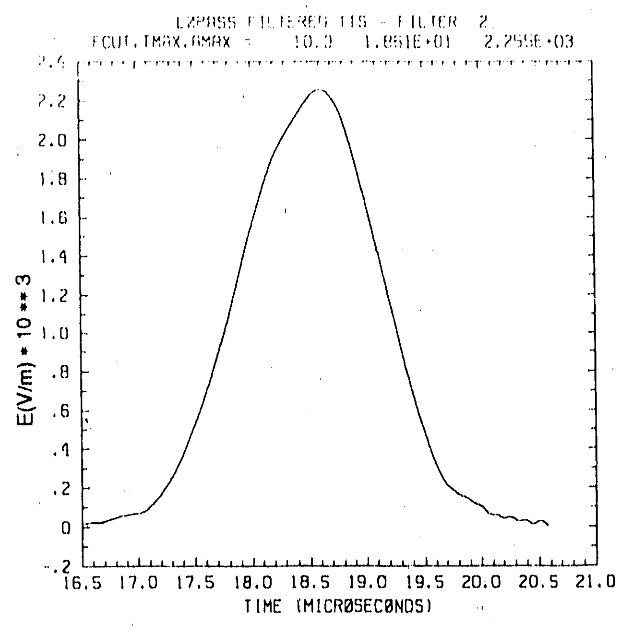

10h

Figures 10e–h: Envelopes of the detected transionospheric signal for the HPD pulse at 20° elevation and 37° azimuth for the 5 and 20 MHz bandwidth receivers centered at 120 MHz and for TECs of 5.0×10^{17} m^{-2} (e and f), and 20.0×10^{17} m^{-2} (g and h).

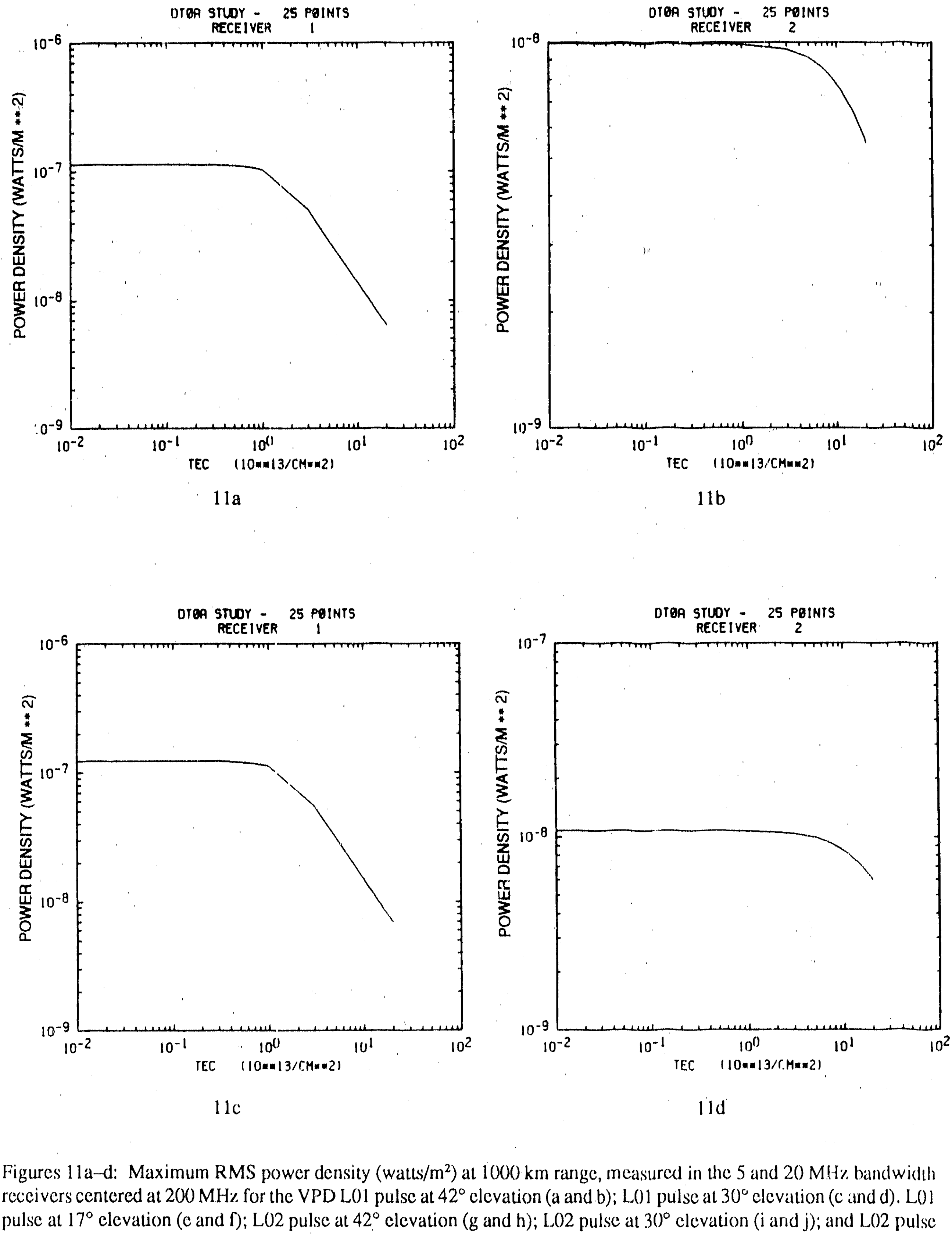

Figures 11a–d: Maximum RMS power density (watts/m^2) at 1000 km range, measured in the 5 and 20 MHz bandwidth receivers centered at 200 MHz for the VPD L01 pulse at 42° elevation (a and b); L01 pulse at 30° elevation (c and d). L01 pulse at 17° elevation (e and f); L02 pulse at 42° elevation (g and h); L02 pulse at 30° elevation (i and j); and L02 pulse at 17° elevation (k and l).

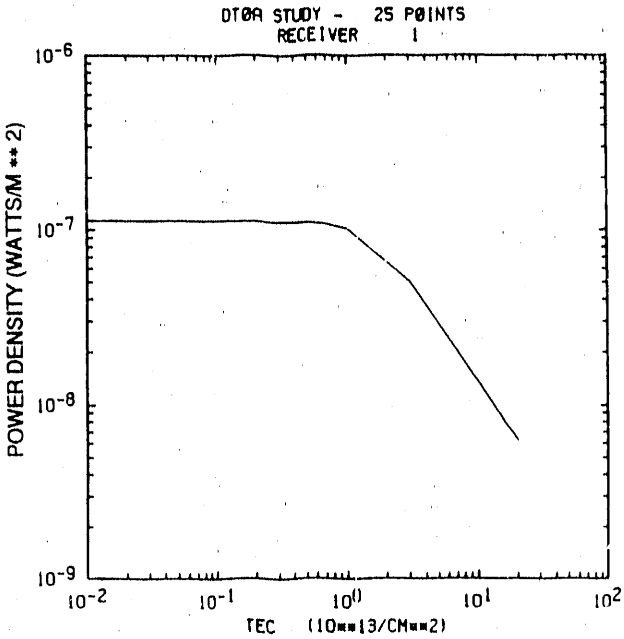

11e

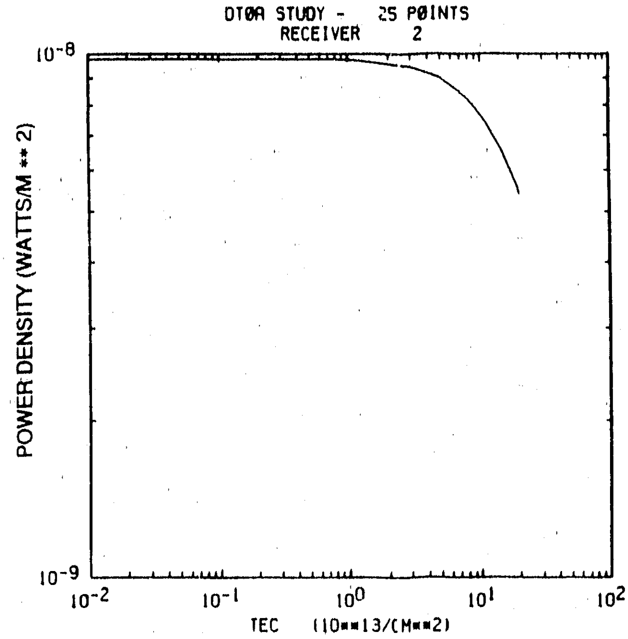

11f

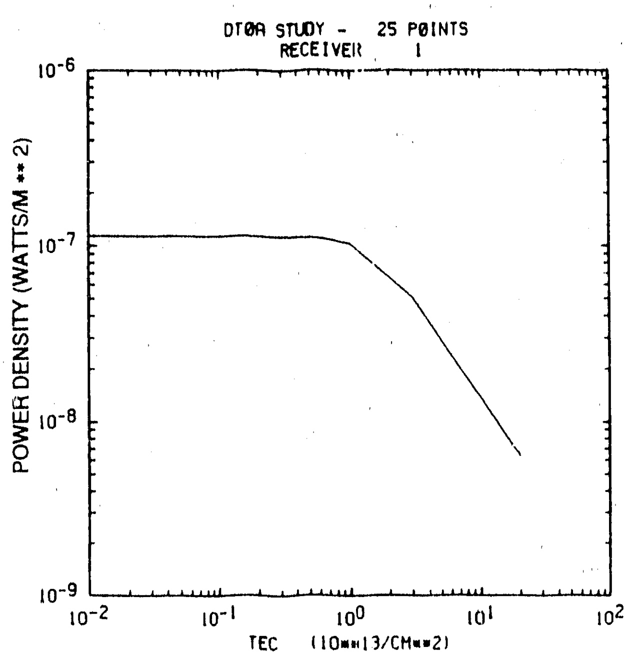

11g

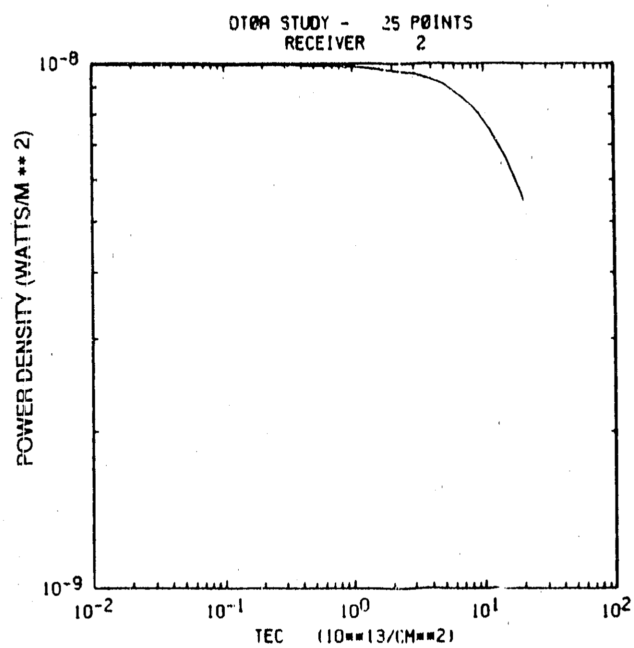

11h

Figures 11e–h: Maximum RMS power density (watts/m^2) at 1000 km range, measured in the 5 and 20 MHz bandwidth receivers centered at 200 MHz for the VPD L01 pulse at 17° elevation (e and f); L02 pulse at 42° elevation (g and h). L02 pulse at 30° elevation (i and j); and L02 pulse at 17° elevation (k and l).

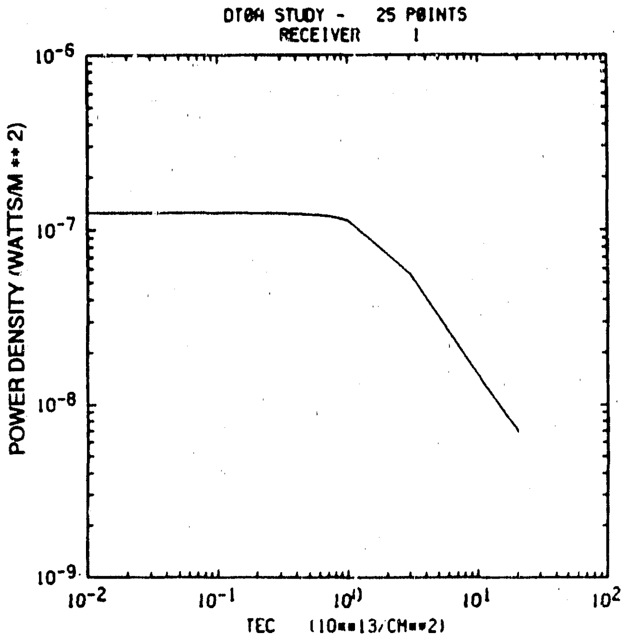

11i

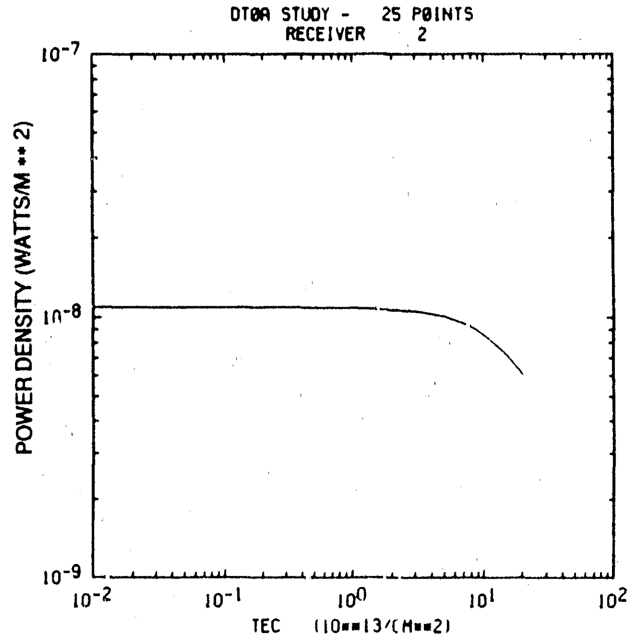

11j

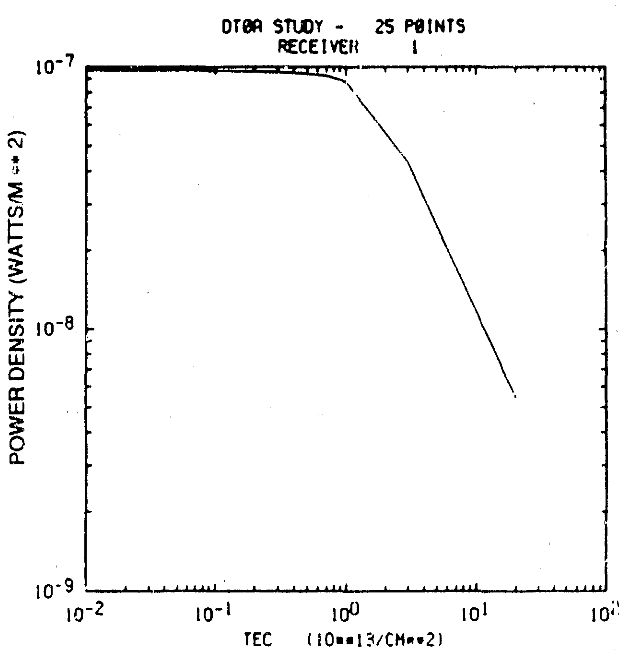

11k

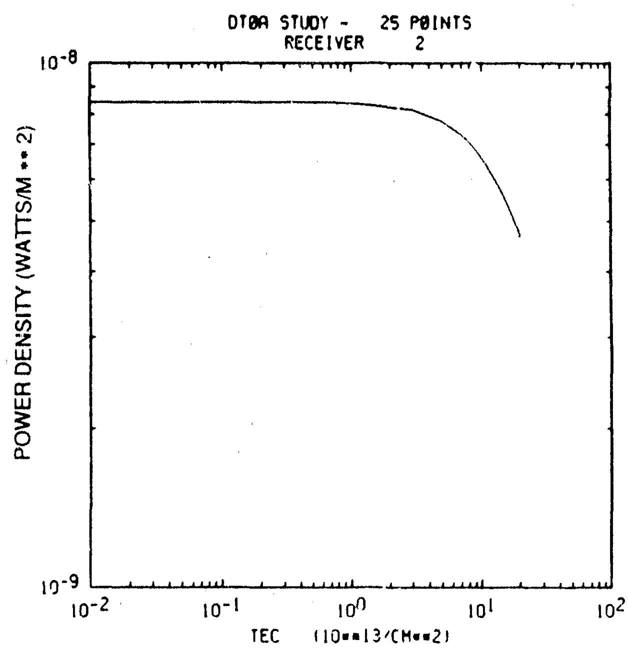

11l

Figures 11i–l: Maximum RMS power density (watts/m^2) at 1000 km range, measured in the 5 and 20 MHz bandwidth receivers centered at 200 MHz for the L02 pulse at 30° elevation (i and j); and L02 pulse at 17° elevation (k and l).

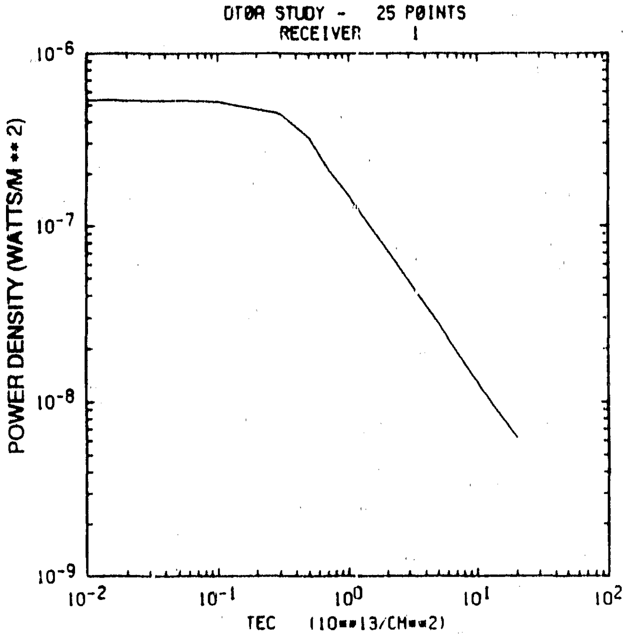

12a

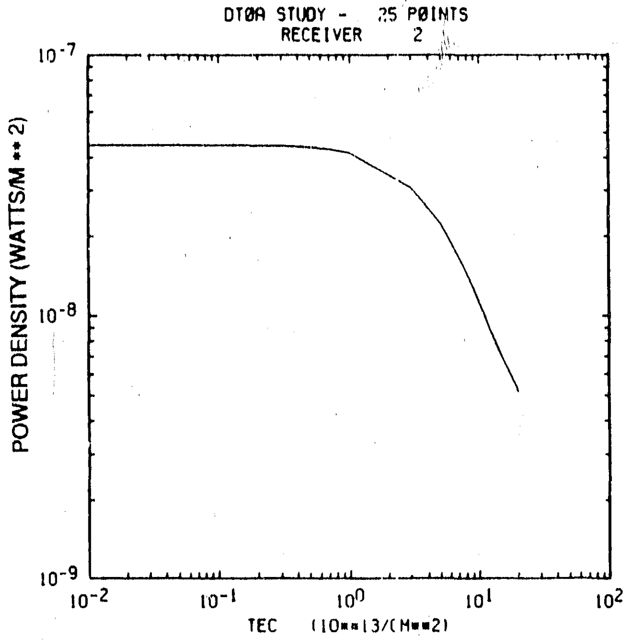

12b

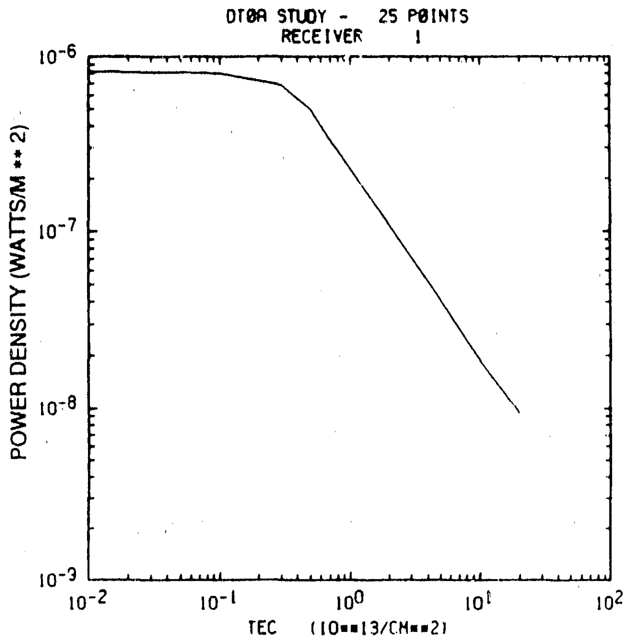

12c

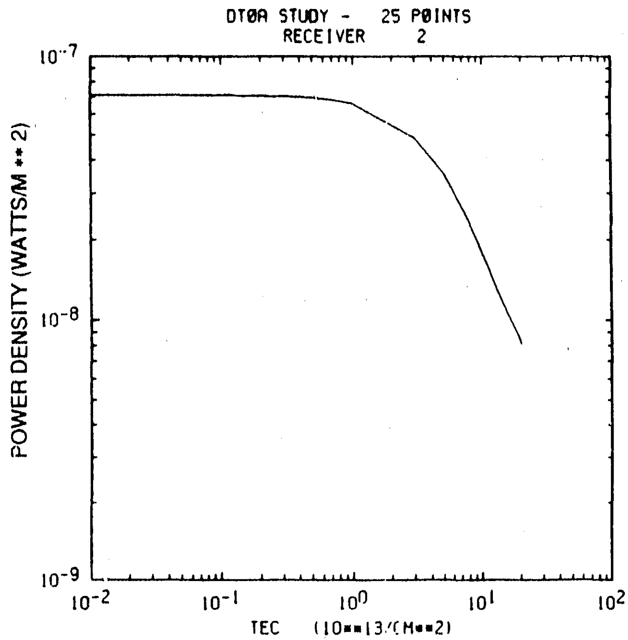

12d

Figures 12a–d: Maximum RMS power density (watts/m^2) at 1000 km range, measured in the 5 and 20 MHz bandwidth receivers centered at 120 MHz for the VPD L01 pulse at 42° elevation (a and b); L01 pulse at 30° elevation (c and d); L01 pulse at 17° elevation (e and f); L02 pulse at 42° elevation (g and h); L02 pulse at 30° elevation (i and j); and L02 pulse at 17° elevation (k and l).

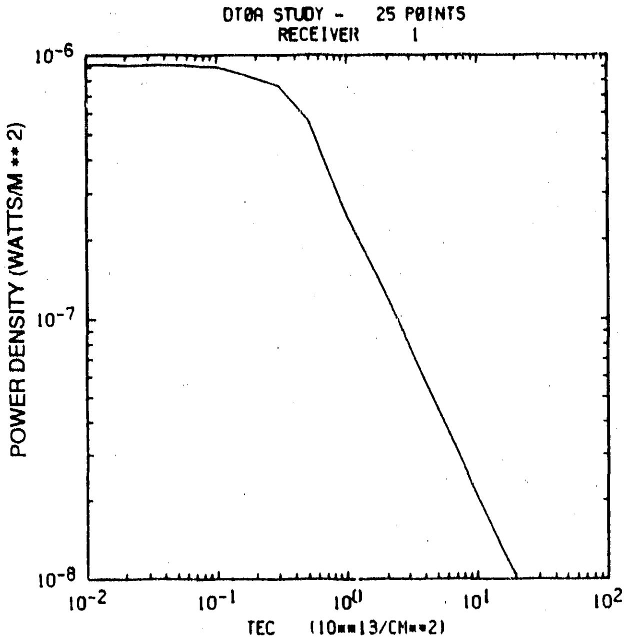

12e

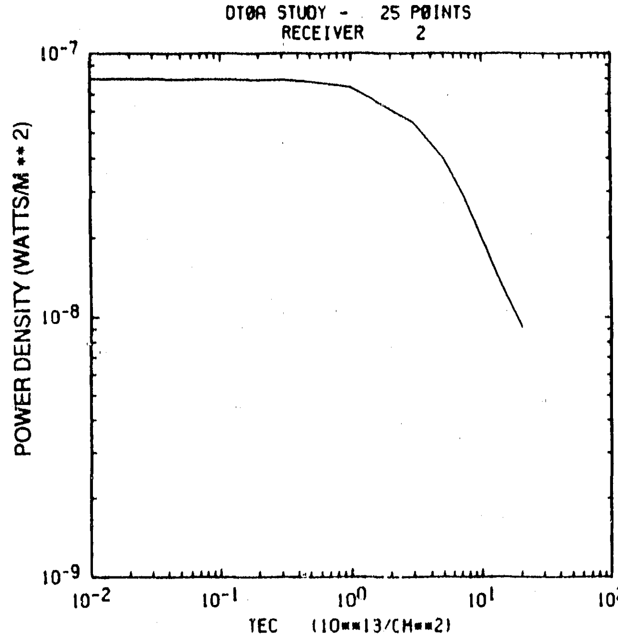

12f

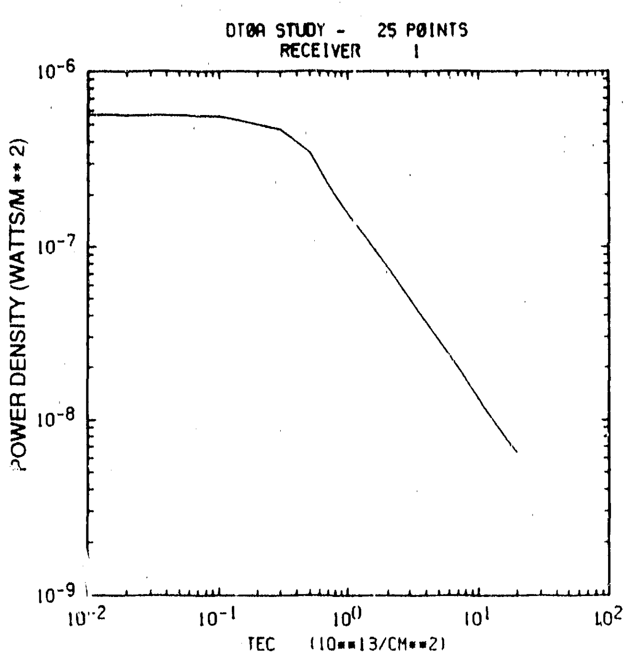

12g

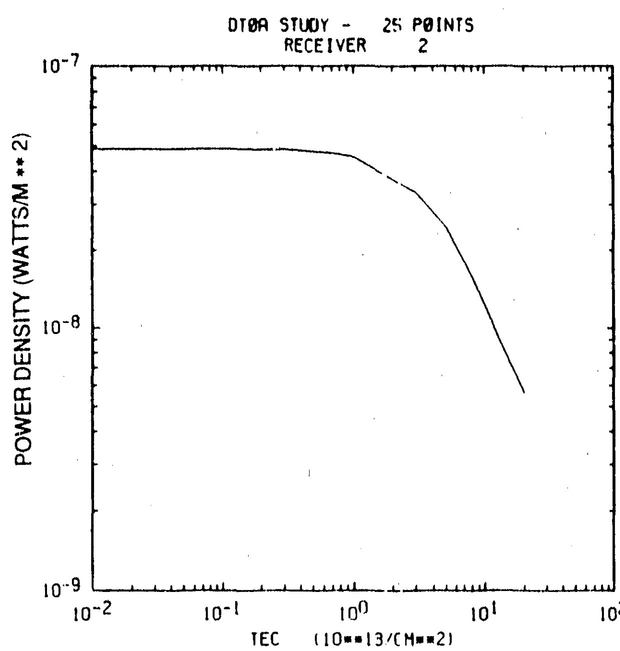

12h

Figures 12e–h: Maximum RMS power density (watts/m^2) at 1000 km range, measured in the 5 and 20 MHz bandwidth receivers centered at 120 MHz for the L01 pulse at 17° elevation (e and f); L02 pulse at 42° elevation (g and h).

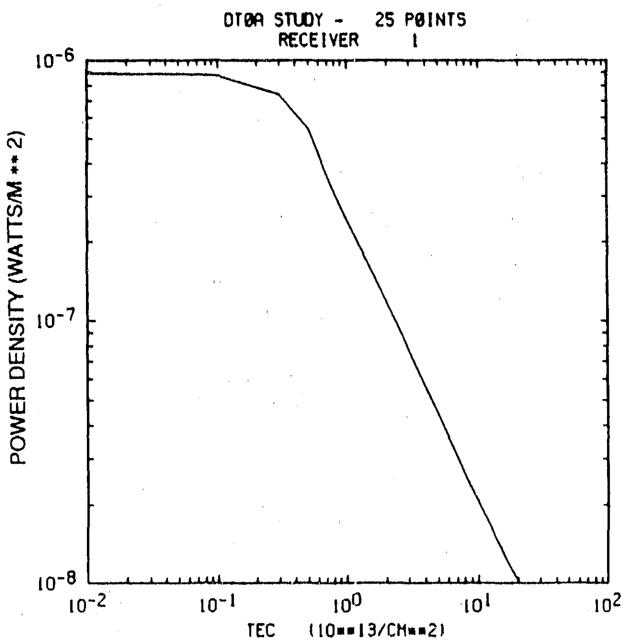

12i

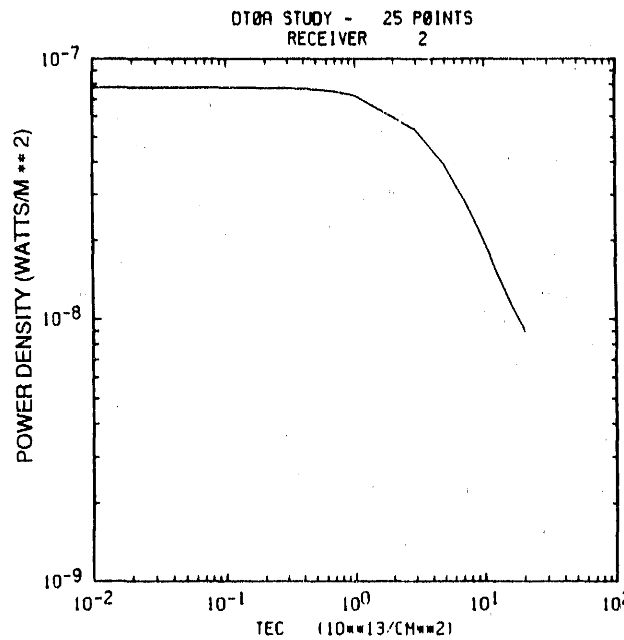

12j

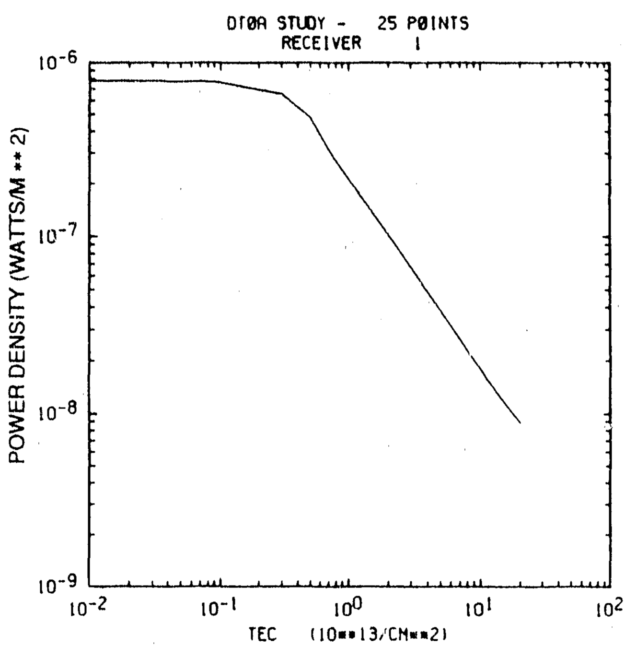

12k

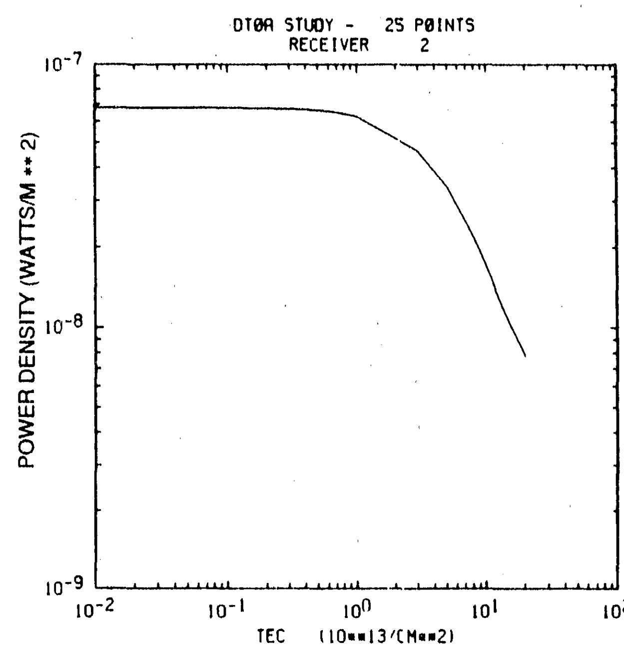

12l

Figures 12i–l: Maximum RMS power density (watts/m^2) at 1000 km range, measured in the 5 and 20 MHz bandwidth receivers centered at 120 MHz for the L02 pulse at 30° elevation (i and j); and L02 pulse at 17° elevation (k and l).

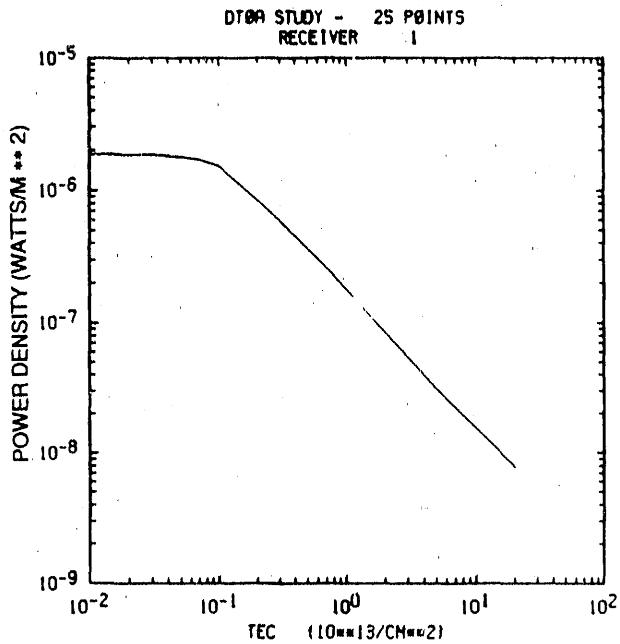

13a

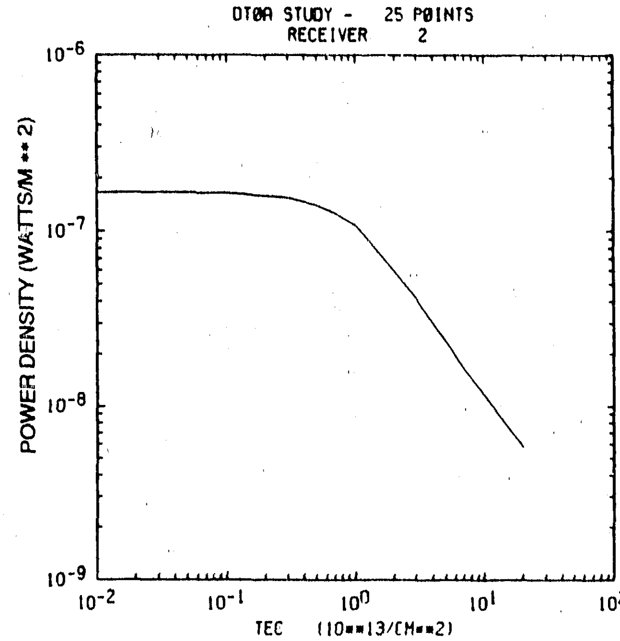

13b

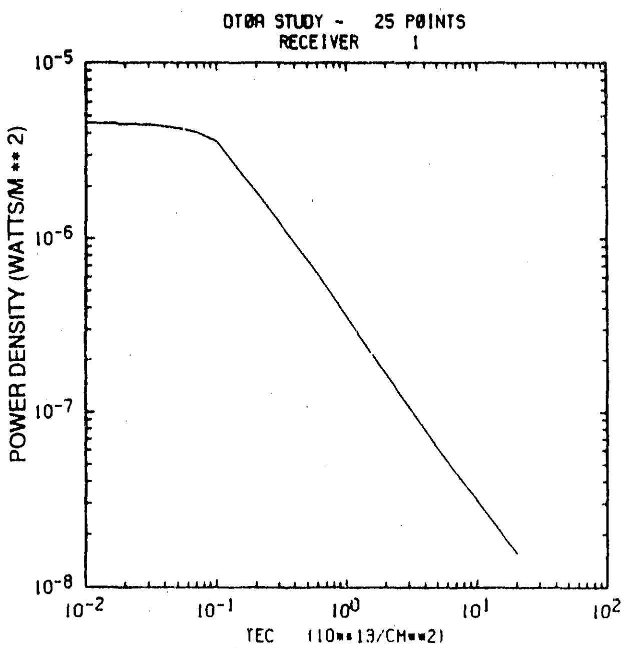

13c

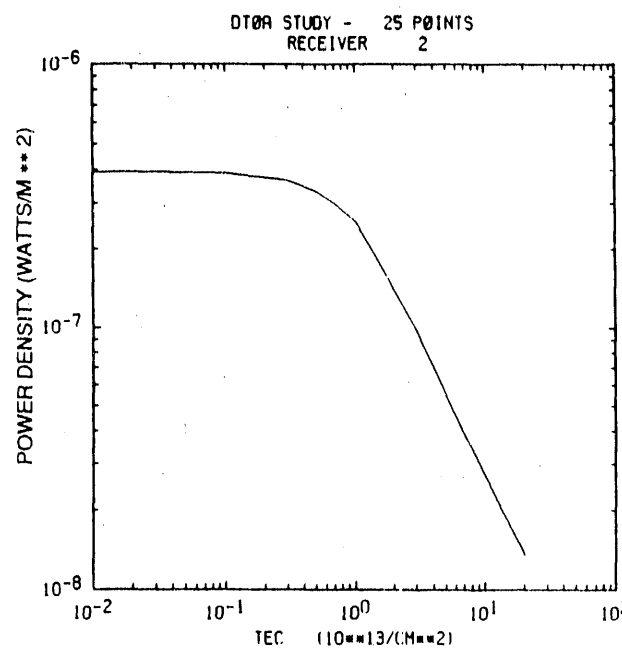

13d

Figures 13a–d: Maximum RMS power density (Watts/m^2) at 1000 km range, measured in the 5 and 20 MHz bandwidth receivers centered at 80 MHz for the VPD L01 pulse at 42° elevation (a and b); L01 pulse at 30° elevation (c and d).

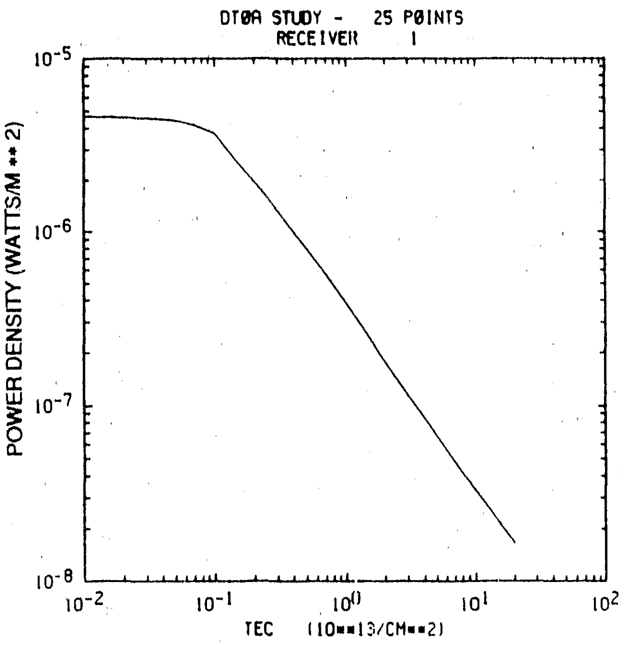

13e

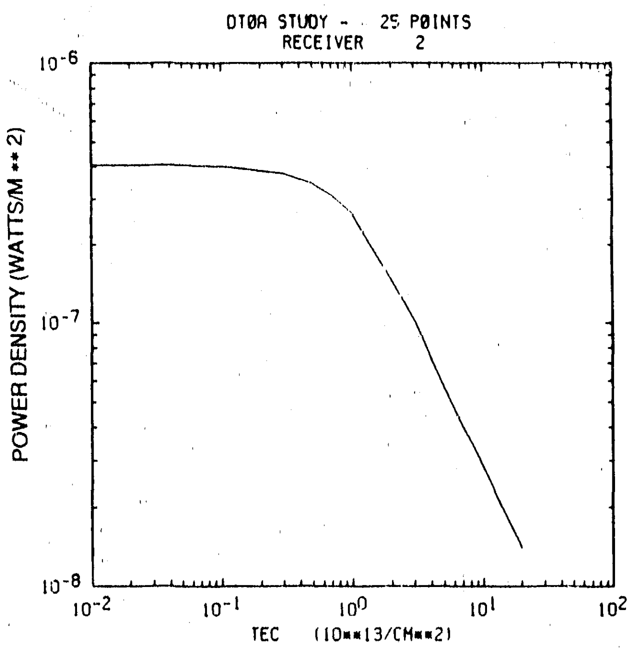

13f

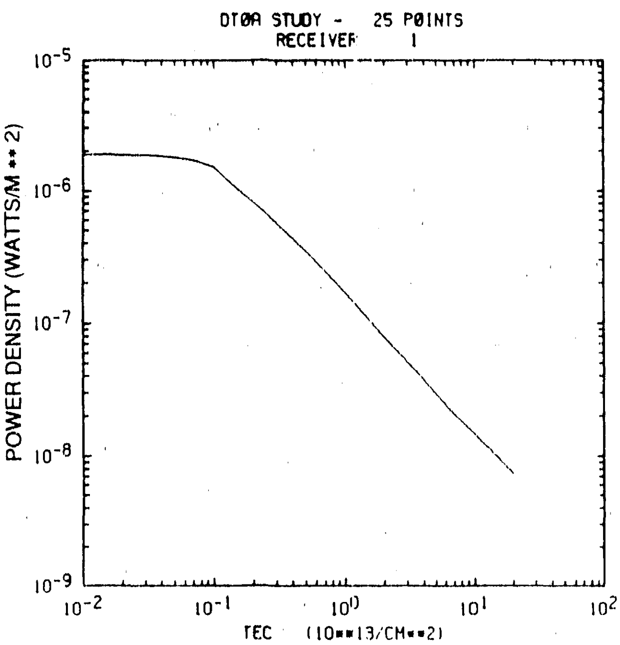

13g

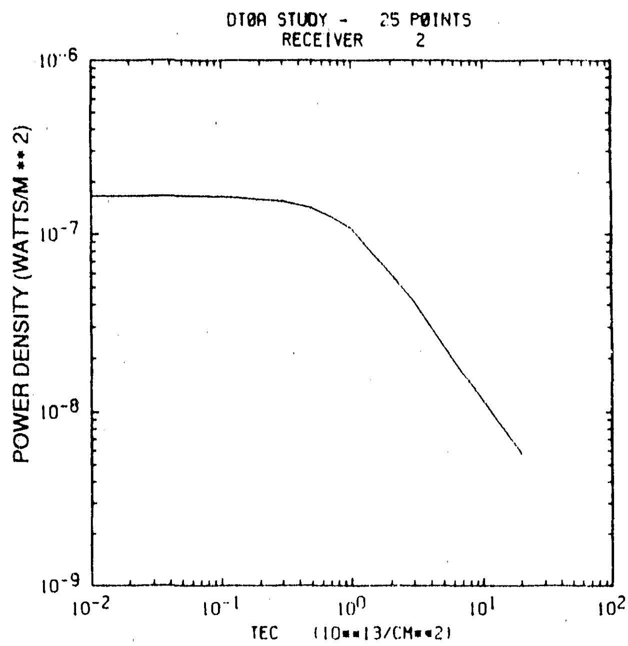

13h

Figures 13e–h Maximum RMS power density (Watts/m^2) at 1000 km range, measured in the 5 and 20 MHz bandwidth receivers centered at 80 MHz for the L01 pulse at 17° elevation (e and f); L02 pulse at 42° elevation (g and h).

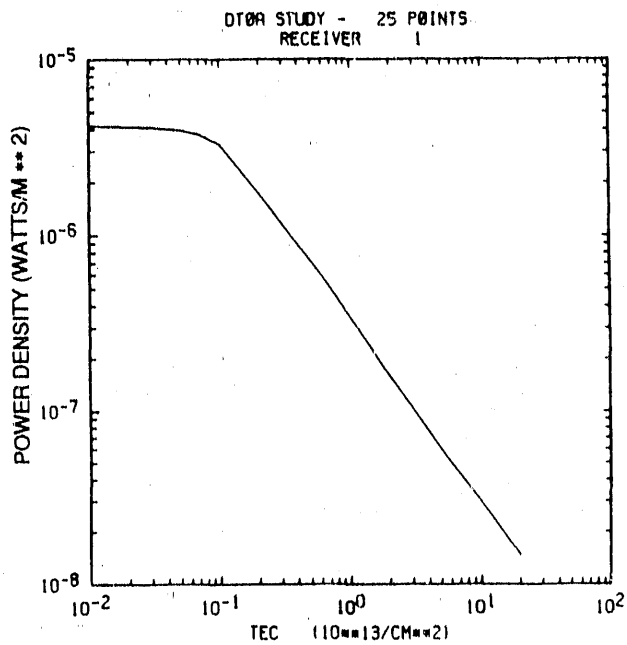

13i

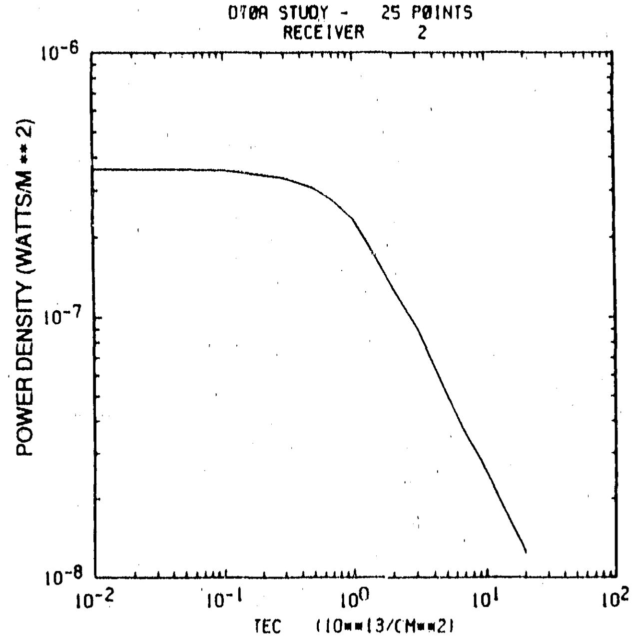

13j

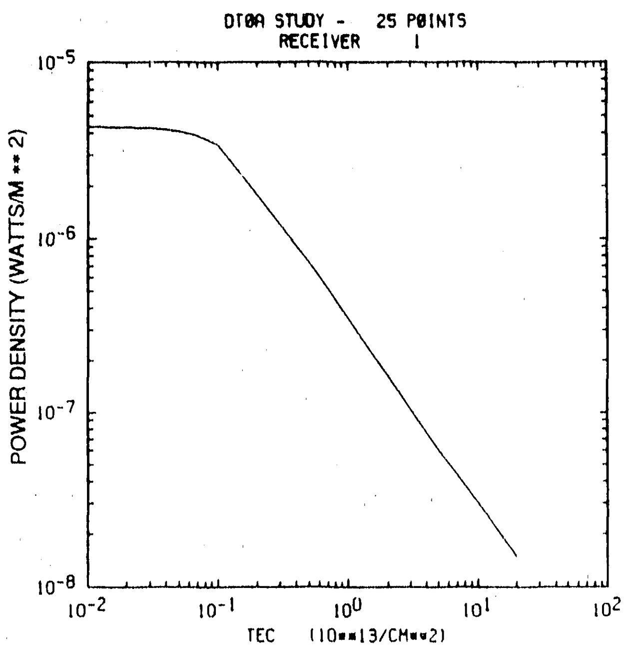

13k

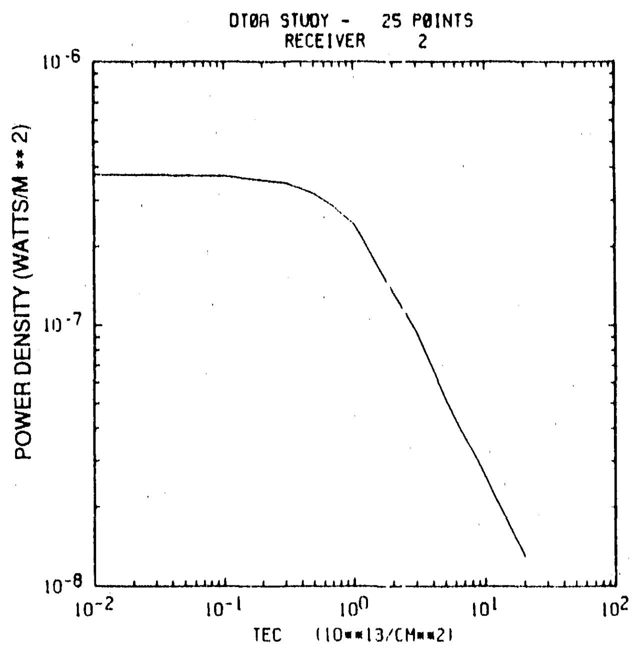

13l

Figures 13i–l: Maximum RMS power density (Watts/m^2) at 1000 km range, measured in the 5 and 20 MHz bandwidth receivers centered at 80 MHz for the L02 pulse at 30° elevation (i and j); and L02 pulse at 17° elevation (k and l).

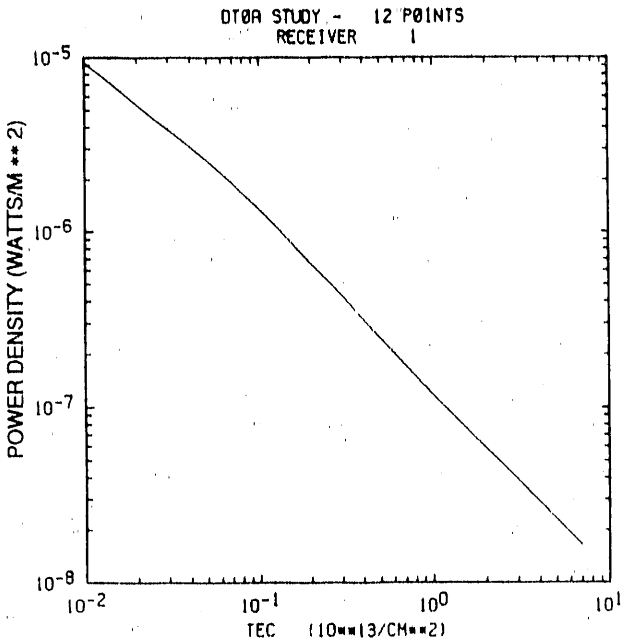

14a

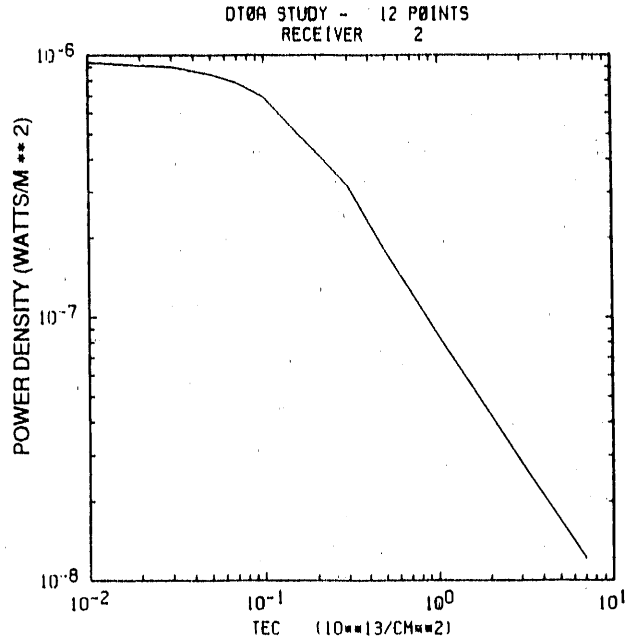

14b

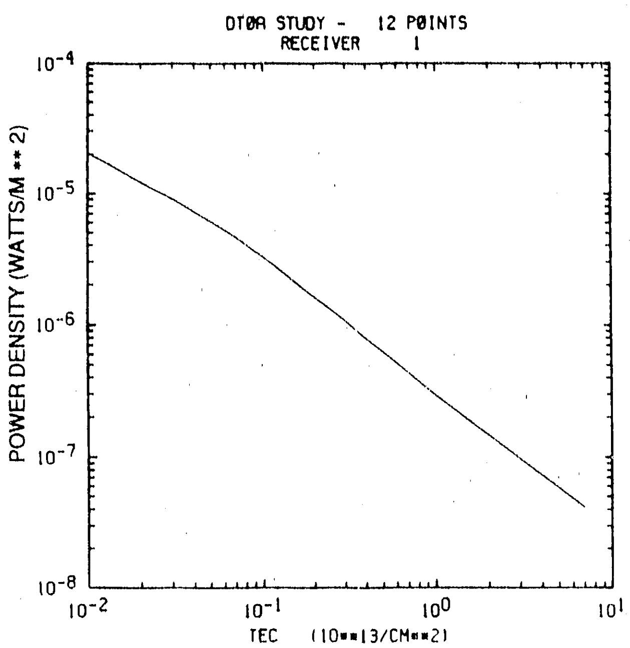

14c

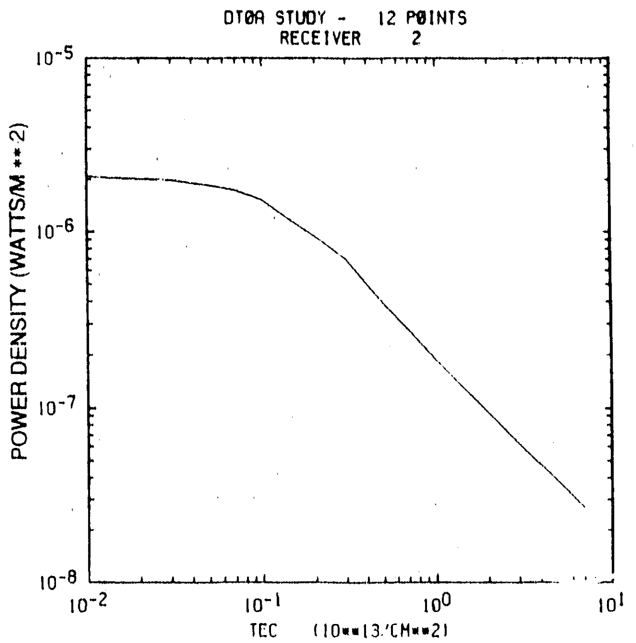

14d

Figures 14a–d: Maximum RMS power density (watts/m²) at 1000 km range, measured in the 5 and 20 MHz bandwidth receivers centered at 40 MHz for the VPD L01 pulse at 42° elevation (a and b); L01 pulse at 30° elevation (c and d).

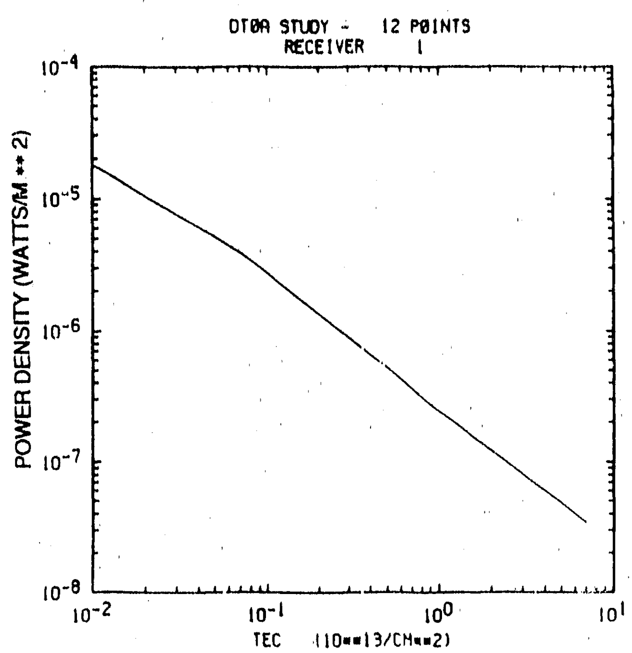

14e

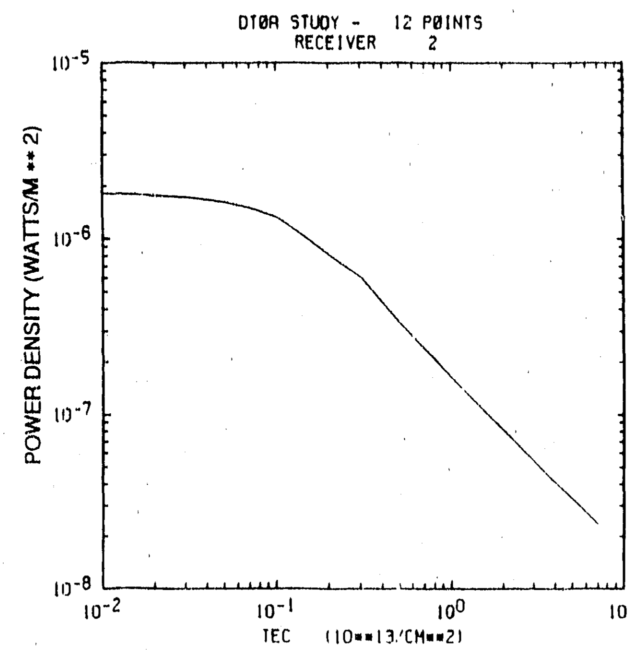

14f

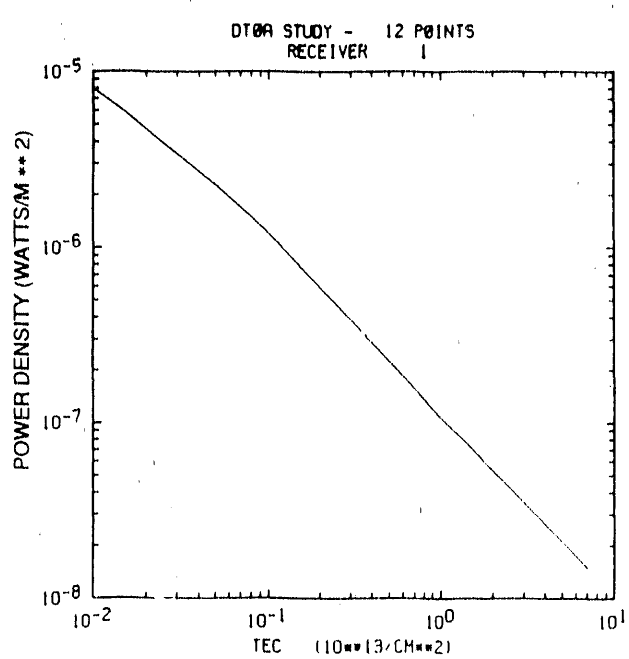

14g

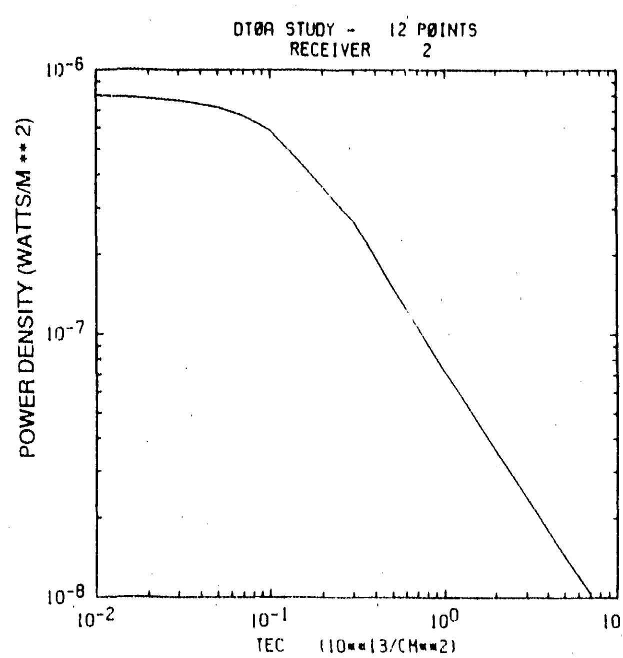

14h

Figures 14e–h: Maximum RMS power density (watts/m^2) at 1000 km range, measured in the 5 and 20 MHz bandwidth receivers centered at 40 MHz for the L01 pulse at 17° elevation (e and f); L02 pulse at 42° elevation (g and h).

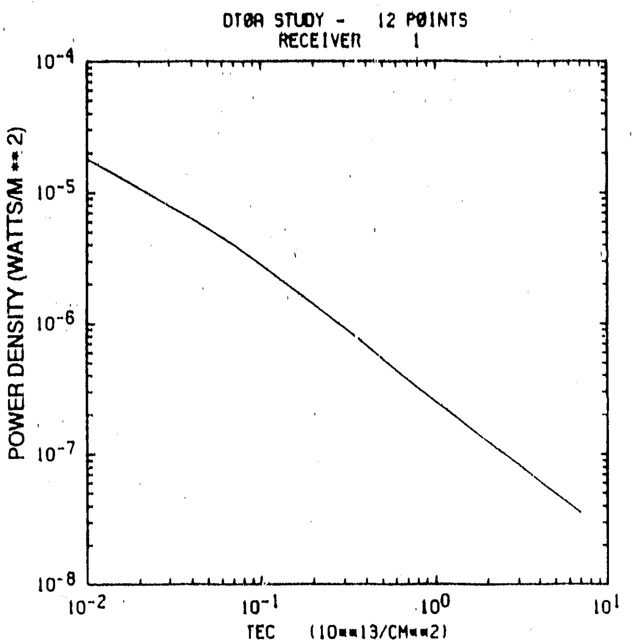

14i

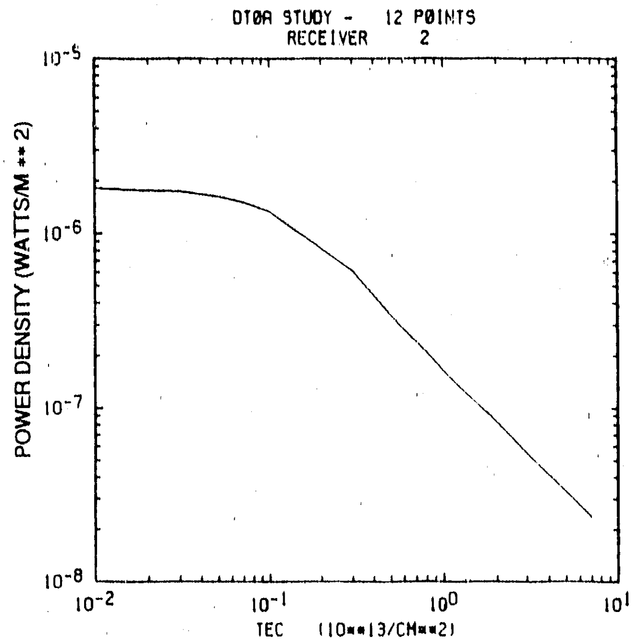

14j

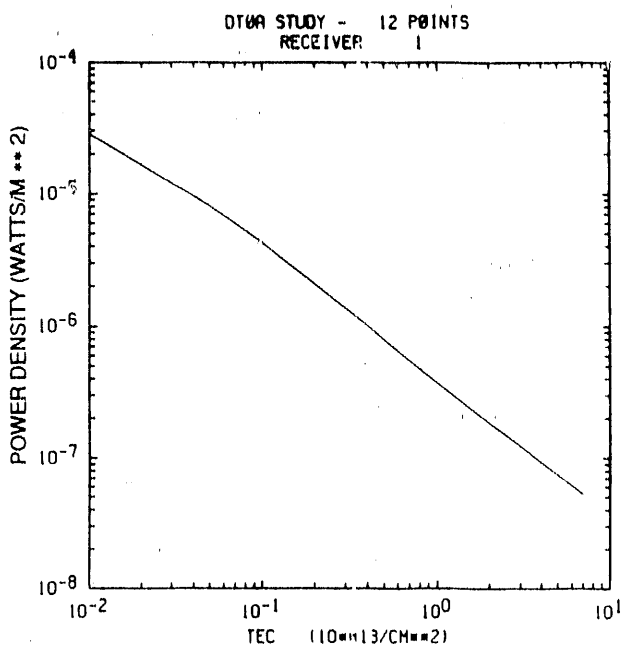

14k

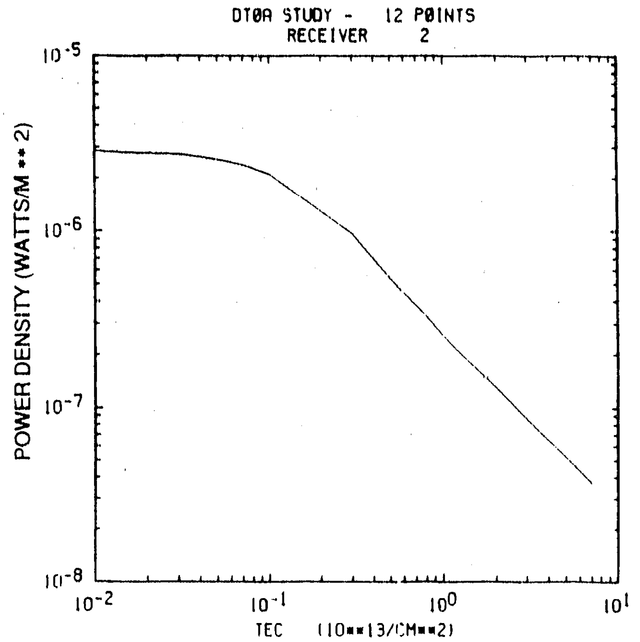

14l

Figures 14i–l: Maximum RMS power density (watts/m²) at 1000 km range, measured in the 5 and 20 MHz bandwidth receivers centered at 40 MHz for the L02 pulse at 30° elevation (i and j); and L02 pulse at 17° elevation (k and l).

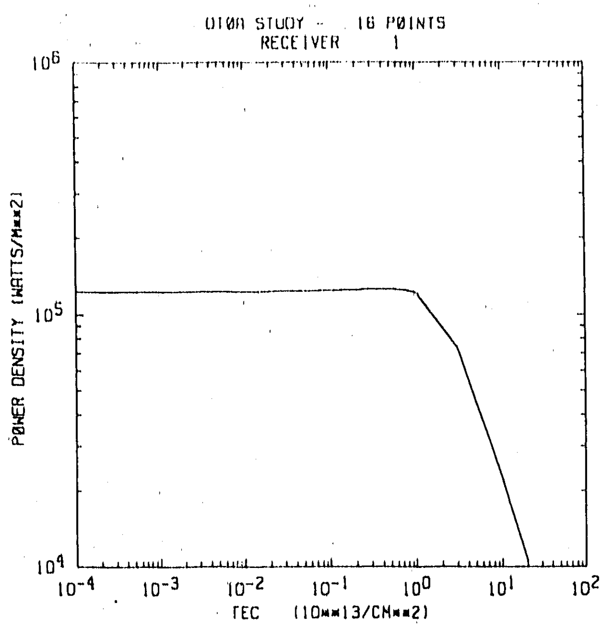

15a

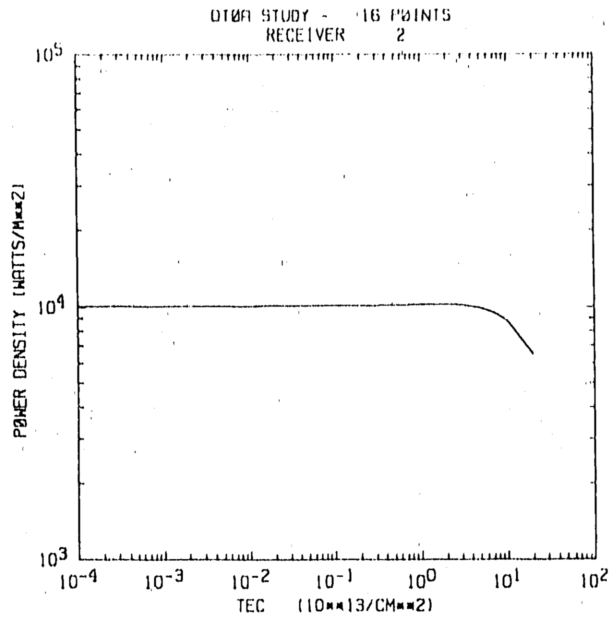

15b

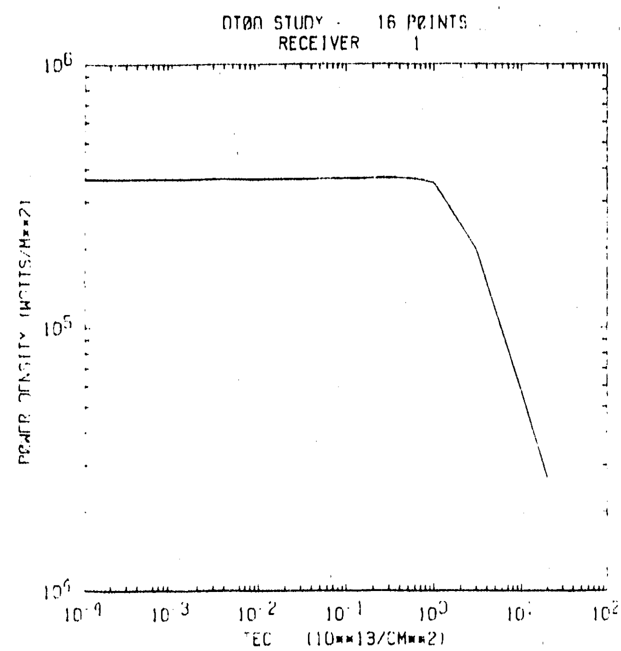

15c

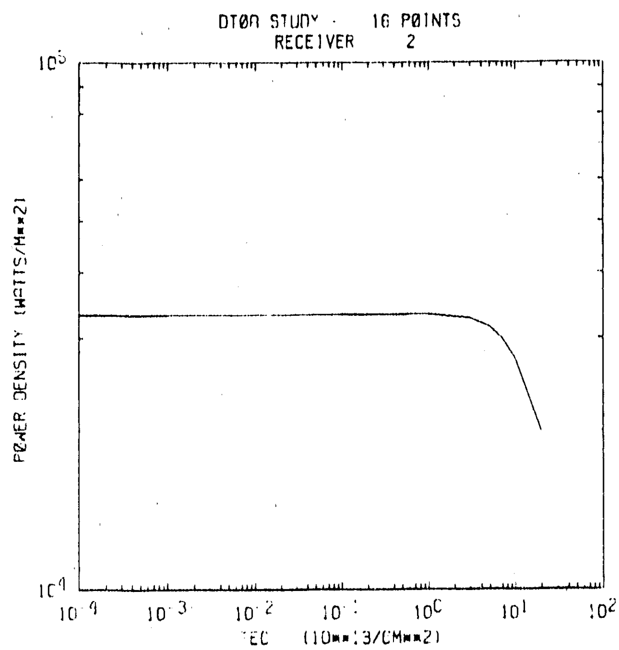

15d

Figures 15a–d: Maximum RMS power density (watts/m^2) at 1 m range, measured in the 5 and 20 MHz bandwidth receivers centered at 200 MHz for the HPD pulse at 20° elevation and 37° azimuth (a and b); and HPD pulse at 20° elevation and 90° azimuth (c and d).

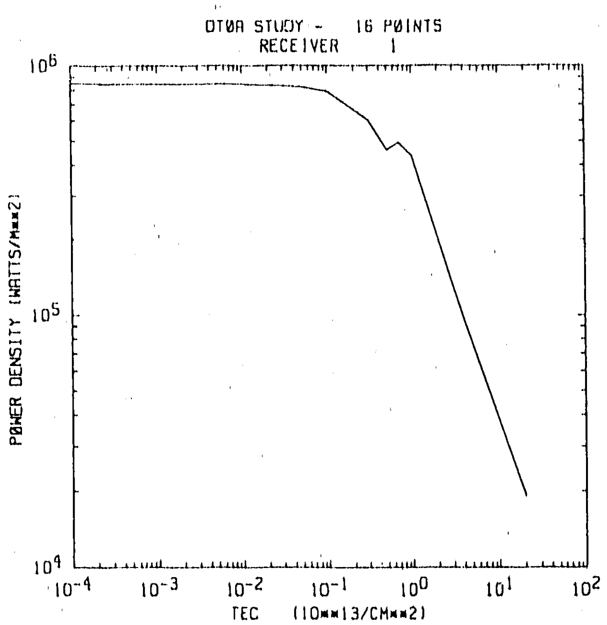

16a

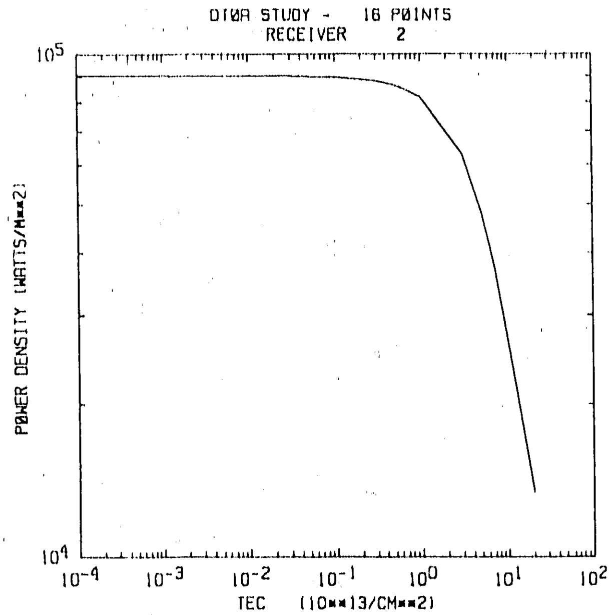

16b

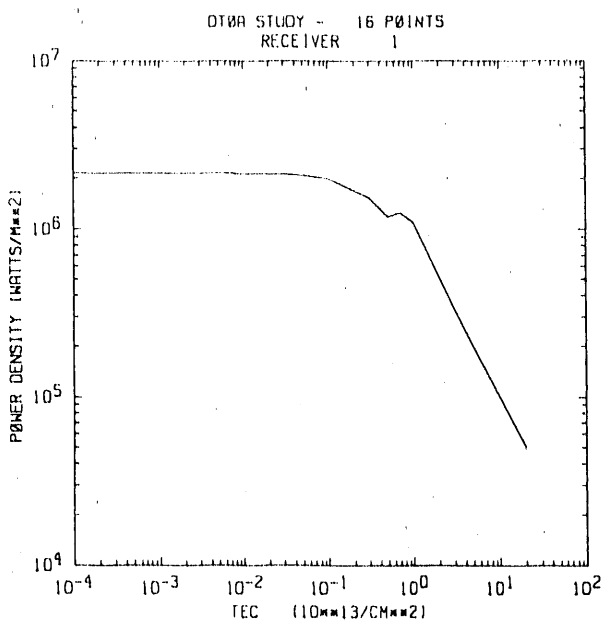

16c

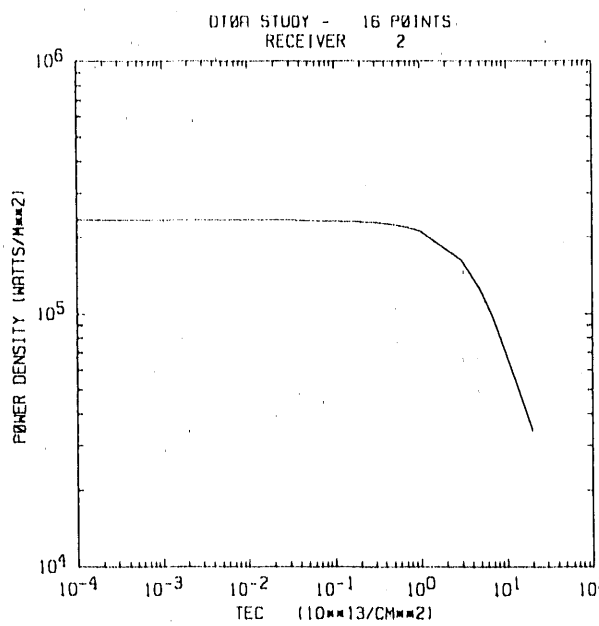

16d

Figures 16a–d: Maximum RMS power density (watts/m^2) at 1 km range, measured in the 5 and 20 MHz bandwidth receivers centered at 120 MHz for the HPD pulse at 20° elevation and 37° azimuth (a and b); and HPD pulse at 20° elevation and 90° azimuth (c and d).

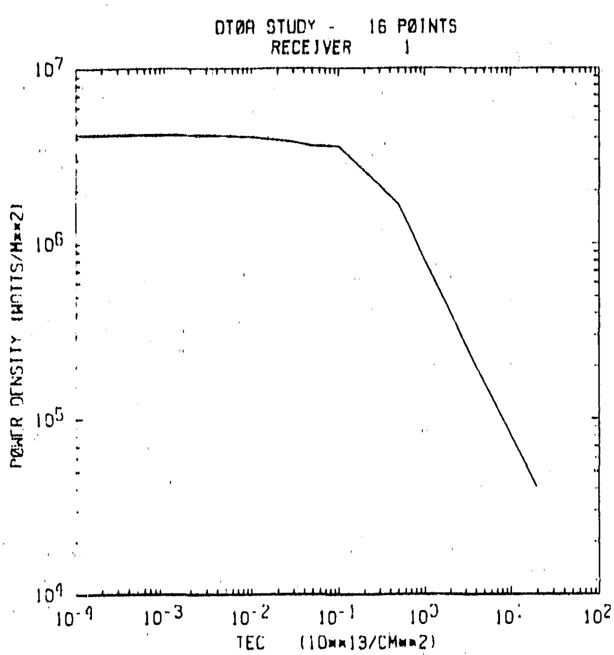

17a

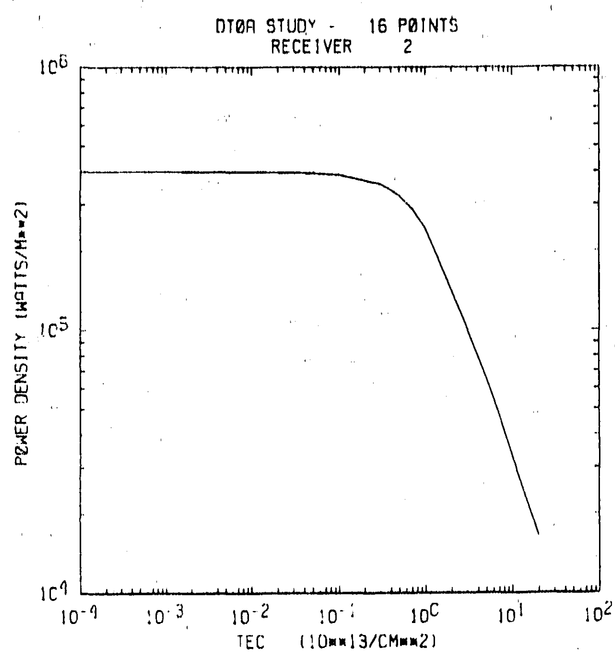

17b

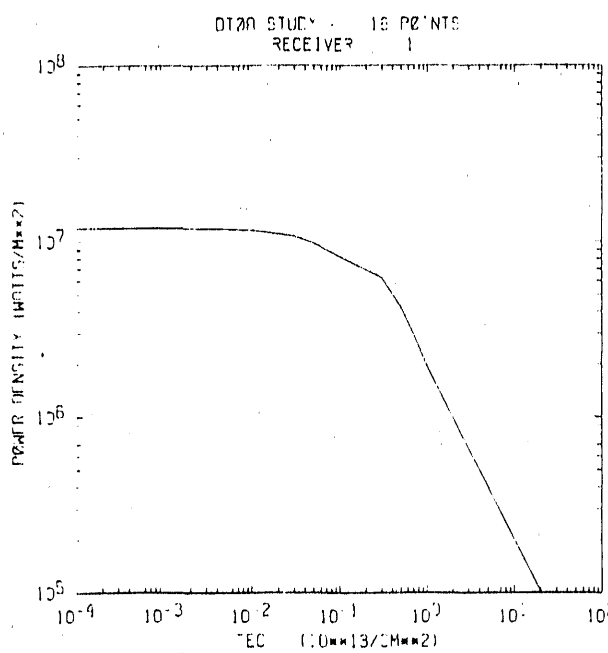

17c

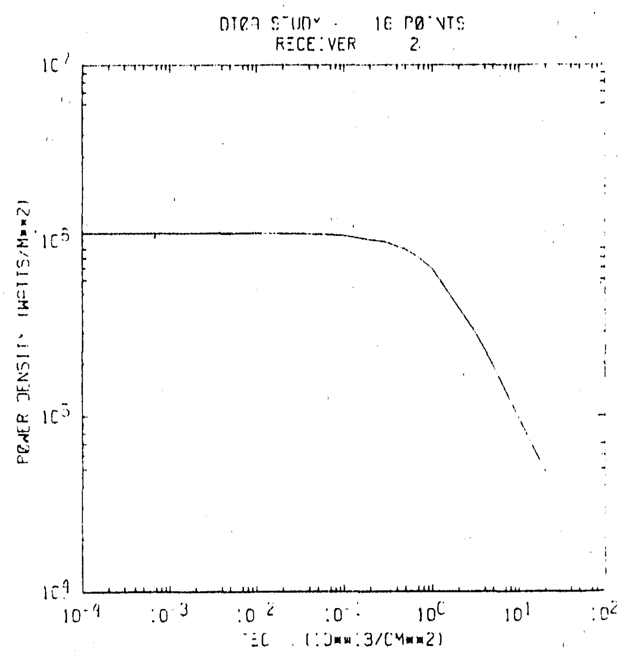

17d

Figures 17a–d: Maximum RMS power density (watts/m²) at 1 m range, measured in the 5 and 20 MHz bandwidth receivers centered at 80 MHz for the HPD pulse at 20° elevation and 37° azimuth (a and b); and HPD pulse at 20° elevation and 90° azimuth (c and d).

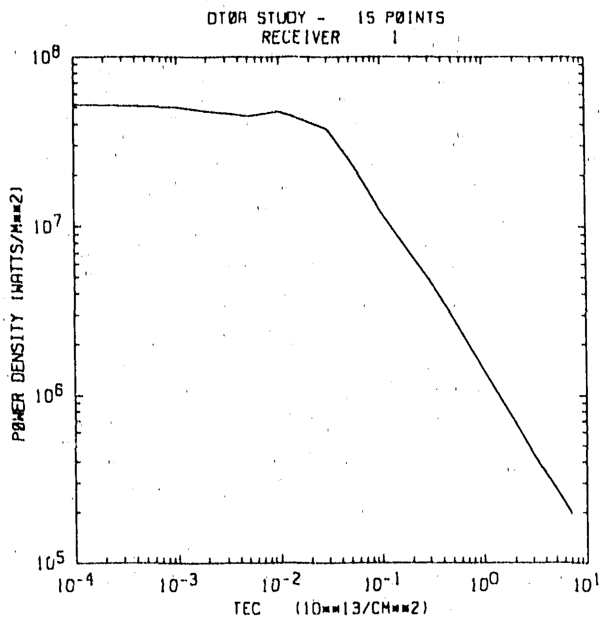

18a

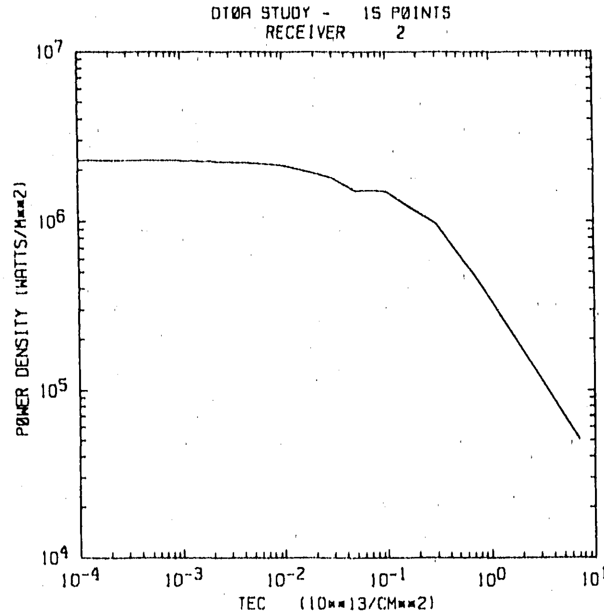

18b

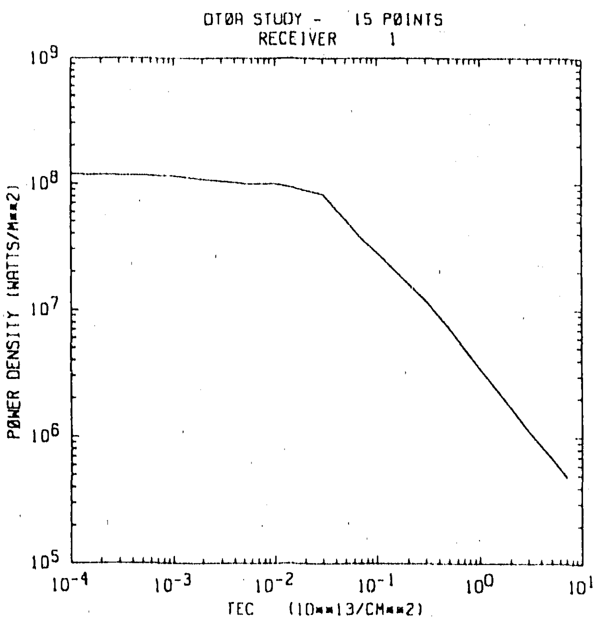

18c

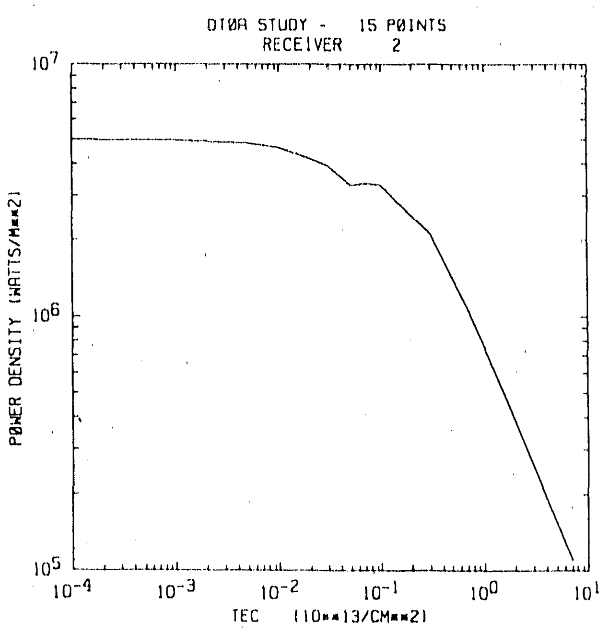

18d

Figures 18a–d: Maximum RMS power density (watts/m^2) at 1 m range, measured in the 5 and 20 MHz bandwidth receivers centered at 40 MHz for the HPD pulse at 20° elevation and 37° azimuth (a and b); and HPD pulse at 20°elevation and 90° azimuth (c and d).

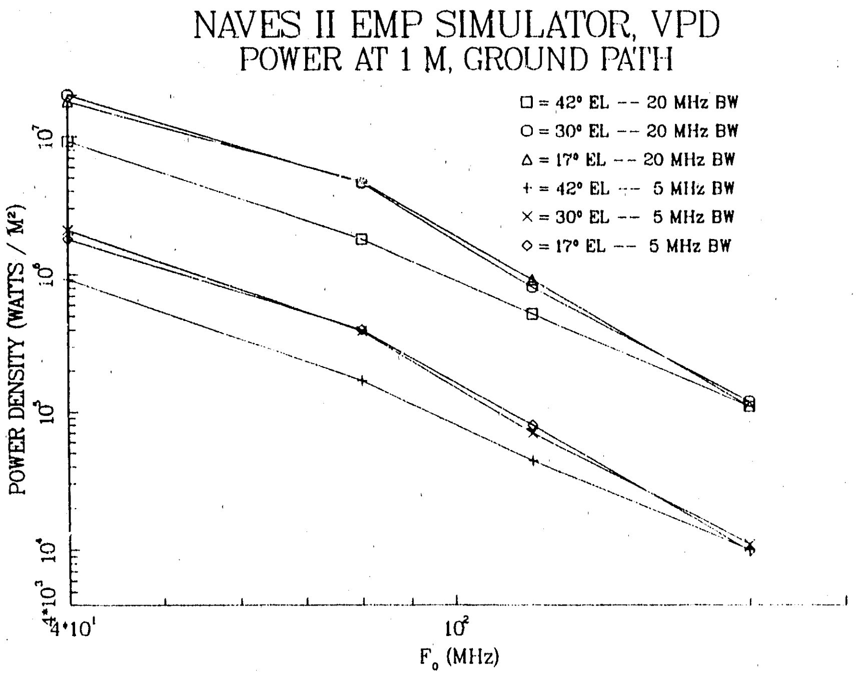

19a

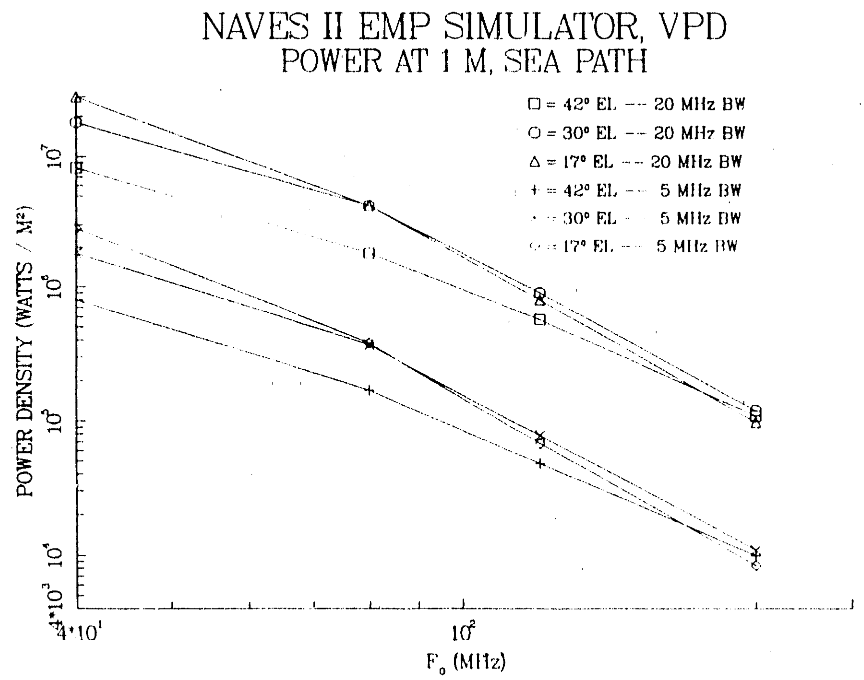

19b

Figures 19a–b: Maximum RMS power density (watts/m^2) at 1 m range, measured in 5 and 20 MHz bandwidth receivers as a function of frequency for the VPD pulse at 42°, 30°, and 17° elevation and for a ground path (19a) and a sea path (19b).

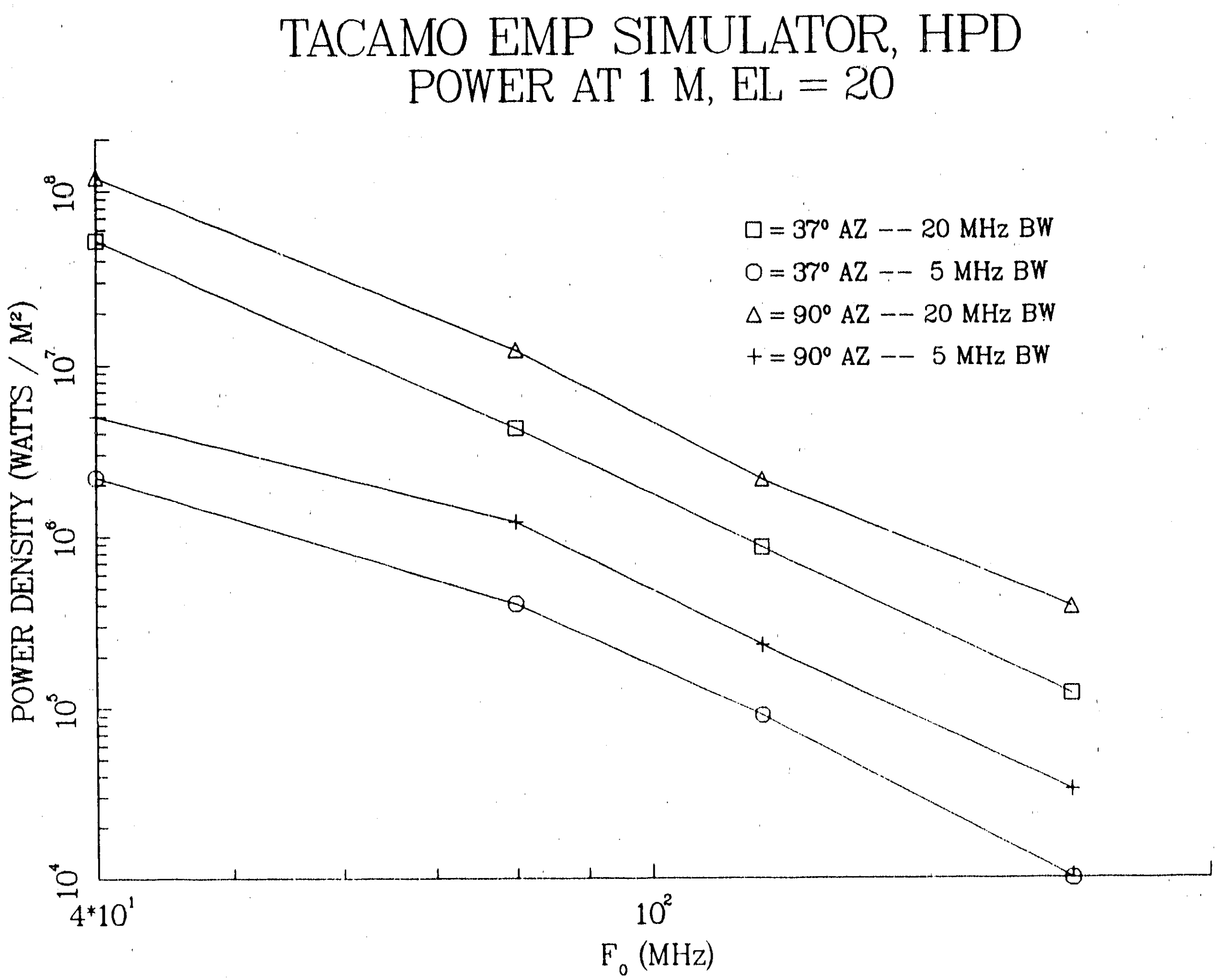

Figure 20: Maximum RMS power density (watts/m²) at 1 m range, measured in 5 and 20 MHz bandwidth receivers as a function of frequency for the HPD pulse at 20° elevation and 37° and 90° azimuth measured relative to the axis of the simulator.

END

DATE FILMED

11 / 21 / 90